

NASA/CR-2002-211449  
ICASE Report No. 2002-1



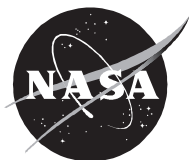
## **Uncertainty Analysis for Fluid Mechanics with Applications**

*Robert W. Walters*

*Virginia Polytechnic Institute and State University, Blacksburg, Virginia*

*Luc Huyse*

*Southwest Research Institute, San Antonio, Texas*



---

February 2002

## Report Documentation Page

<b>Report Date</b> 00FEB2002	<b>Report Type</b> N/A	<b>Dates Covered (from... to)</b> -
<b>Title and Subtitle</b> Uncertainty Analysis for Fluid Mechanics with Applications	<b>Contract Number</b>	
	<b>Grant Number</b>	
	<b>Program Element Number</b>	
<b>Author(s)</b> Robert W. Walters, Luc Huyse	<b>Project Number</b>	
	<b>Task Number</b>	
	<b>Work Unit Number</b>	
<b>Performing Organization Name(s) and Address(es)</b> ICASE Mail Stop 132C NASA Langley Research Center Hampton, VA 23681-2199	<b>Performing Organization Report Number</b>	
<b>Sponsoring/Monitoring Agency Name(s) and Address(es)</b>	<b>Sponsor/Monitor's Acronym(s)</b>	
	<b>Sponsor/Monitor's Report Number(s)</b>	
<b>Distribution/Availability Statement</b> Approved for public release, distribution unlimited		
<b>Supplementary Notes</b> ICASE Report No. 2002-1		
<b>Abstract</b> See Document		
<b>Subject Terms</b>		
<b>Report Classification</b> unclassified	<b>Classification of this page</b> unclassified	
<b>Classification of Abstract</b> unclassified	<b>Limitation of Abstract</b> SAR	
<b>Number of Pages</b> 50		

## The NASA STI Program Office . . . in Profile

Since its founding, NASA has been dedicated to the advancement of aeronautics and space science. The NASA Scientific and Technical Information (STI) Program Office plays a key part in helping NASA maintain this important role.

The NASA STI Program Office is operated by Langley Research Center, the lead center for NASA's scientific and technical information. The NASA STI Program Office provides access to the NASA STI Database, the largest collection of aeronautical and space science STI in the world. The Program Office is also NASA's institutional mechanism for disseminating the results of its research and development activities. These results are published by NASA in the NASA STI Report Series, which includes the following report types:

- **TECHNICAL PUBLICATION.** Reports of completed research or a major significant phase of research that present the results of NASA programs and include extensive data or theoretical analysis. Includes compilations of significant scientific and technical data and information deemed to be of continuing reference value. NASA's counterpart of peer-reviewed formal professional papers, but having less stringent limitations on manuscript length and extent of graphic presentations.
- **TECHNICAL MEMORANDUM.** Scientific and technical findings that are preliminary or of specialized interest, e.g., quick release reports, working papers, and bibliographies that contain minimal annotation. Does not contain extensive analysis.
- **CONTRACTOR REPORT.** Scientific and technical findings by NASA-sponsored contractors and grantees.

- **CONFERENCE PUBLICATIONS.** Collected papers from scientific and technical conferences, symposia, seminars, or other meetings sponsored or cosponsored by NASA.
- **SPECIAL PUBLICATION.** Scientific, technical, or historical information from NASA programs, projects, and missions, often concerned with subjects having substantial public interest.
- **TECHNICAL TRANSLATION.** English-language translations of foreign scientific and technical material pertinent to NASA's mission.

Specialized services that complement the STI Program Office's diverse offerings include creating custom thesauri, building customized data bases, organizing and publishing research results . . . even providing videos.

For more information about the NASA STI Program Office, see the following:

- Access the NASA STI Program Home Page at <http://www.sti.nasa.gov>
- Email your question via the Internet to [help@sti.nasa.gov](mailto:help@sti.nasa.gov)
- Fax your question to the NASA STI Help Desk at (301) 621-0134
- Telephone the NASA STI Help Desk at (301) 621-0390
- Write to:  
NASA STI Help Desk  
NASA Center for Aerospace Information  
7121 Standard Drive  
Hanover, MD 21076-1320

NASA/CR-2002-211449  
ICASE Report No. 2002-1



## **Uncertainty Analysis for Fluid Mechanics with Applications**

*Robert W. Walters*

*Virginia Polytechnic Institute and State University, Blacksburg, Virginia*

*Luc Huyse*

*Southwest Research Institute, San Antonio, Texas*

*ICASE*

*NASA Langley Research Center*

*Hampton, Virginia*

*Operated by Universities Space Research Association*



---

February 2002

---

Available from the following:

NASA Center for AeroSpace Information (CASI)  
7121 Standard Drive  
Hanover, MD 21076-1320  
(301) 621-0390

National Technical Information Service (NTIS)  
5285 Port Royal Road  
Springfield, VA 22161-2171  
(703) 487-4650

# UNCERTAINTY ANALYSIS FOR FLUID MECHANICS WITH APPLICATIONS

ROBERT W. WALTERS\* AND LUC HUYSE†

**Abstract.** This paper reviews uncertainty analysis methods and their application to fundamental problems in fluid dynamics. Probabilistic (Monte-Carlo, Moment methods, Polynomial Chaos) and non-probabilistic methods (Interval Analysis, Propagation of error using sensitivity derivatives) are described and implemented. Results are presented for a model convection equation with a source term, a model non-linear convection-diffusion equation; supersonic flow over wedges, expansion corners, and an airfoil; and two-dimensional laminar boundary layer flow.

**Key words.** stochastic, probabilistic, uncertainty, error

**Subject classification.** Applied and Numerical Mathematics

**1. Introduction and Motivation.** In the past few years, there has been numerous papers appearing in the Computational Fluid Dynamics (CFD) literature addressing the subject of credible CFD simulations (see [1], [2], [6], [7], [10], [21], [30], [33], [35], [36], [38], [39], [41], [42], [49]). In fact, the May 1998 issue of the AIAA Journal devoted a special section on the topic. Among the key issues discussed in that section were: Code Verification, Code Validation, Certification and Sources of Uncertainty. One of the primary reasons for the increased interest in uncertainty management is its application in risk-based design methods. The structures community and dynamics and controls discipline have a long history in uncertainty analysis whereas the computational fluid dynamics community is a newcomer in this area due in part to the relative infancy of the discipline and in part to the large cost of CFD simulations. However, with the increase in computing power and software improvements over the past two decades, stochastic CFD is coming of age. Consequently, the primary purpose of this paper is to serve as an introductory guide for engineers with an interest in fluid dynamics applications of uncertainty analysis methods.

Before proceeding to review the basic methods, some discussion on nomenclature is warranted. In this paper we adopt the AIAA definitions for error and uncertainty [3], namely:

**DEFINITION 1.1.** *Error: A recognizable deficiency in any phase or activity of modeling and simulation that is not due to lack of knowledge.*

**DEFINITION 1.2.** *Uncertainty: A potential deficiency in any phase or activity of the modeling process that is due to lack of knowledge.*

These definitions recognize the deterministic nature of error and the stochastic nature of uncertainty. Uncertainty can be further categorized into aleatoric (or inherent uncertainty) and epistemic (or model) uncertainty. Further categorizations are possible and discussed in [29]. This report focuses on methods for describing and propagating parameter uncertainty in models. In a companion report [29], we describe methods for dealing with model form and boundary condition uncertainty for the non-linear Burgers equation.

---

\*Virginia Polytechnic Institute and State University, Department of Aerospace and Ocean Engineering, Blacksburg, VA 24061-0203 (email: walters@aoe.vt.edu). This research was supported by the National Aeronautics and Space Administration under NASA Contract No. NAS1-97046 while the author was in residence at ICASE, NASA Langley Research Center, Hampton, VA 23681-2199.

†Southwest Research Institute, Reliability and Engineering Mechanics, San Antonio, TX 78228 (email: lhuyse@swri.edu). This research was supported by the National Aeronautics and Space Administration under NASA Contract No. NAS1-97046 while the author was in residence at ICASE, NASA Langley Research Center, Hampton, VA 23681-2199.

TABLE 1.1

*Source of Uncertainty and Error in CFD Simulations - summarized from Oberkampf and Blottner, Ref. [35]*

Source	Examples
<b>Physical Modeling</b> (Assumptions in the PDE)	Inviscid Flow Viscous Flow Incompressible Flow Chemically Reacting Gas Transitional/Turbulent Flow
<i>Auxiliary Physical Models</i>	Equation of State Thermodynamic properties Transport properties Chemical models, reactions, and rates Turbulence model
<i>Boundary Conditions</i>	Wall, e.g. roughness Open, e.g. far-field Free Surface Geometry Representation
<b>Discretization &amp; Solution</b>	Truncation error - spatial and temporal Iterative convergence - steady state Iterative convergence - time dependent Geometry Representation
<b>Round-Off Error</b>	Finite - precision arithmetic
<b>Programming &amp; User Error</b>	

In some instances in this report, we have used a more general definition of uncertainty that includes error where it is clear that no ambiguity arises.

In the AIAA special issue, Oberkampf and Blottner [36] group sources of uncertainty and error arising from the simulation of physical phenomena governed by PDE's into four broad categories:

1. Physical modeling
2. Discretization and solution errors
3. Computer round-off error
4. Programming errors

An examination of Table 1.1 shows that many sources of error and uncertainty arise in CFD simulations. It is generally believed that discretization error, geometric uncertainty and turbulence model uncertainty are the largest sources of uncertainty in modern Reynolds-Averaged Navier-Stokes simulations and collectively account for much of the scatter observed between experimental and computational data [2]. Discretization error has been studied extensively and a number of techniques have been proposed for modeling this error (see e.g. [40], [41], [43]). Grid adaptation schemes frequently use these models for improving the base grid. The impact of geometric uncertainty has been studied by Darmofal [13] for compressor blades using probabilistic methods. Although relatively little has been done for quantifying turbulence model uncertainty, there has been some work in this area [8], [20]. More recently, Godfrey [19] used the continuous sensitivity equation approach to rank the relative importance of the closure coefficients in three turbulence models:

the Baldwin-Lomax algebraic model, the Spalart-Allmaras one-equation model and the Wilcox two-equation  $k - \omega$  turbulence model.

With the present state of computational resources, some sources of error can be made negligible. For example, for essentially all one- and two-dimensional steady, inviscid or laminar flows, a user typically has sufficient hardware to drive the discretization error to very low levels, essentially zero, leaving model uncertainty as the only significant source of uncertainty. Over time, this trend will continue and eventually encompass a large class of three-dimensional simulations. However, without further research effort concentrated on uncertainty estimation and management, model uncertainty will likely remain relatively constant over time since it is not a known error that can simply be reduced with additional computing power.

In the next section, we review methods that can be used in CFD simulations for dealing with error and uncertainty. Next, a range of problems starting with some simple model problems and ending with laminar boundary layer flow are presented.

**2. Review of Uncertainty Analysis Methods.** In this section, we briefly review deterministic and probabilistic methods for uncertainty analysis. Two deterministic uncertainty analysis methods - 1) Interval Analysis and 2) Propagation of error using sensitivity derivatives and three probabilistic methods 1) Monte Carlo, 2) Moment methods, and 3) Polynomial Chaos are summarized below.

**2.1. Interval Analysis.** The basic idea in interval analysis is to perform operations on input intervals that contain the set of all possible values of the input in such a way that the output interval consists of all possible values of the result of the operations performed on the input. Consequently, interval results represent maximal error bounds (i.e., worst case results). One of the most appealing things about Interval Analysis (IA) is that it can be implemented in a systematic way on modern computing systems such that the details of the interval operations are transparent to the user. Thus, one can take an existing simulation tool, such as a CFD code, and immediately implement interval analysis provided that it is supported by the programming environment. However, it should be pointed out that different expressions for computing an interval output quantity can result in different interval widths even if the expressions are mathematically equivalent for pointwise input. To demonstrate this, consider the following two expressions that are equivalent for point values,

$$(2.1) \quad f(x) = \frac{x}{1+x} \quad \text{and} \quad g(x) = \frac{1}{1+\frac{1}{x}}.$$

Table 2.1 shows the results of performing interval analysis for these two functions for input intervals,  $x$ , defined in terms of the interval midpoint value,  $\bar{x}$ , and uncertainty,  $\varepsilon$ , by

$$(2.2) \quad x = \bar{x}[1 - \varepsilon, 1 + \varepsilon].$$

Values in the table correspond to  $\varepsilon = 1/10$ . Note that the interval width associated with the second relation,  $g(x)$ , is substantially smaller than the width found by evaluation of  $f(x)$ . This shows that, although existing software can take immediate advantage of interval analysis, significant improvement in the size of the error bounds may be possible by careful design and construction of the operations within the software. However, this investment may not be prudent since probabilistic methods provide much more information than can be obtained through interval analysis. This example also illustrates one other point: the fact that different interval results can be obtained is not related to the precision of the calculation. Here, rational numbers were used to carry out the operations exactly. Different interval output occurs because set theoretical operations - union, intersection, complement are affected by the *structural form* of the operations.



TABLE 2.1

*Interval analysis results for two simple expressions that are equivalent for point values but not for intervals.*

$\bar{x}$	$x$	$f(\bar{x})$	$g(\bar{x})$	$f(x)$	$g(x)$	$\frac{\ f(x)\ }{\ g(x)\ }$
1	$[\frac{9}{10}, \frac{11}{10}]$	$\frac{1}{2}$	$\frac{1}{2}$	$[\frac{3}{7}, \frac{11}{19}]$	$[\frac{9}{19}, \frac{11}{21}]$	3
$\frac{5}{4}$	$[\frac{9}{8}, \frac{11}{8}]$	$\frac{5}{9}$	$\frac{5}{9}$	$[\frac{9}{19}, \frac{11}{17}]$	$[\frac{9}{17}, \frac{11}{19}]$	$\frac{7}{2}$
$\frac{3}{2}$	$[\frac{27}{20}, \frac{33}{20}]$	$\frac{3}{5}$	$\frac{3}{5}$	$[\frac{27}{53}, \frac{33}{47}]$	$[\frac{27}{47}, \frac{33}{53}]$	4
$\frac{7}{4}$	$[\frac{63}{40}, \frac{77}{40}]$	$\frac{7}{11}$	$\frac{7}{11}$	$[\frac{7}{13}, \frac{77}{103}]$	$[\frac{63}{103}, \frac{77}{117}]$	$\frac{9}{2}$
2	$[\frac{9}{5}, \frac{11}{5}]$	$\frac{2}{3}$	$\frac{2}{3}$	$[\frac{9}{16}, \frac{11}{14}]$	$[\frac{9}{14}, \frac{11}{16}]$	5

Moreover, interval arithmetic inside iteration loops results in error growth each iteration without some modification to the base algorithm (see Section 3). Since many fluid dynamics codes rely on iteration for the solution process, this further detracts from the use of this approach. In a probabilistic modeling, varying degrees of correlation between random variables can readily be taken into account in the analysis. The practical examples of Section 5.2 and 6.2 will illustrate this point and indicate that, depending on the value of the correlation, the uncertainty may be larger or smaller than in the case where all variables are independent. Since interval analysis is a deterministic method, it cannot take advantage of this information and must necessarily compute the widest bounds.

**2.2. Propagation of Error using Sensitivity Derivatives.** Error propagation using sensitivity derivatives has been in use for many years (see e.g. Dahlquist and Björck [9]). If  $u = u(\xi_1, \dots, \xi_n)$  where  $\xi_i$  is the  $i^{th}$  independent variable with error  $\Delta\xi_i$  associated with it, then a deterministic approximation to the error,  $\Delta u$ , is given by

$$(2.3) \quad \Delta u \approx \left[ \sum_{i=1}^n \left( \frac{\partial u}{\partial \xi_i} \right)_i^2 \Delta \xi_i^2 \right]^{\frac{1}{2}}.$$

A computational fluid dynamics example of this technique is presented in the work of Turgeon et. al., [11], in which the laminar flow of corn syrup was analyzed subject to uncertainty in the viscosity model, the thermal conductivity model, the geometry, and the boundary conditions. In their work, they used the continuous sensitivity equation method (see Section 4) to evaluate the sensitivity derivatives,  $\frac{\partial u}{\partial \xi_i}$ , in Eq.(2.3). This results in an error estimate,  $\Delta u$ , which in their work was shown to bound the experimental data. We wish to emphasize that this approach is based on the assumption that a particular input interval (for example, one of their inputs was an experimentally measured temperature,  $T \pm 2\%$ ), contains the *entire* uncertainty interval due to this variable. We will contrast this with a probabilistic framework in Section 2.4.

**2.3. Monte Carlo.** Although there are many different applications of Monte Carlo simulation, both deterministic and probabilistic, the focus in this report is on probabilistic simulation methods. A briefly history of the method is given by Hammersley and Handscomb in [24] and summarized here. Arguably, the development of the method and name, Monte Carlo, is considered to have its start around 1944 when von Neumann and Ulam performed direct simulation of neutron transport problems, primarily as a tool for atomic bomb research. Shortly after the end of World War II, Fermi, Ulam, von Neumann and others began applying Monte Carlo methods to deterministic problems. By 1948, Monte Carlo estimates of the eigenvalues of the Schrödinger equation had been obtained. Sometime thereafter, this work came to the attention of Dr. Stephen Brush at the Livermore Laboratory who subsequently unearthed a 1901 paper by Lord Kelvin [31] in which remarkably modern Monte Carlo techniques appear in connection with the Boltzmann equation.

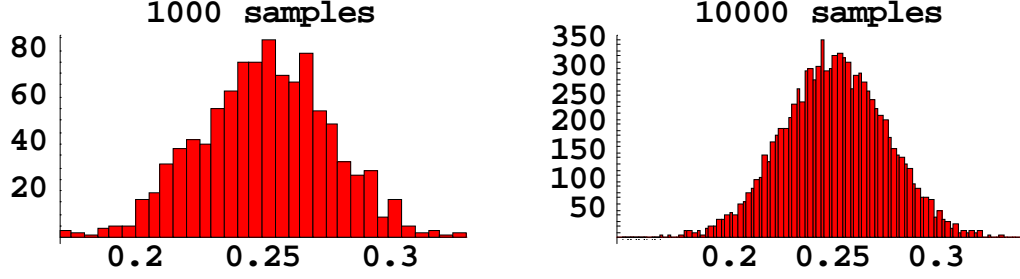


FIG. 2.1. Typical histograms obtained by sampling from a Normal distribution with a mean of 0.25 and a standard deviation of 0.025 corresponding to a coefficient of variation,  $CoV = 10\%$ . Left - 1,000 samples, Right 10,000 samples.

Apparently, the methods were obvious to Lord Kelvin and consequently his focus was on the results. Even prior to this application, there are isolated accounts of the method [23].

Here we demonstrate one of the simplest of all Monte Carlo methods, referred to as crude (or basic) Monte Carlo. In this approach, the basic procedure is:

1. sample input random variable(s) from their known or assumed (joint-) probability density function
2. compute deterministic output for each sampled input value(s)
3. determine statistics of the output distribution, e.g., mean, variance, skewness, ...

The statistics of a distribution (mean, variance, skewness, kurtosis, ...) can be determined from the definition of the expected value of a function of a random variable,  $\xi$ , say  $g(\xi)$ , namely

$$(2.4) \quad \mathbb{E}[g(\xi)] = \int g(\xi)p(\xi)d\xi,$$

where  $p(\xi)$  is the probability density function of the distribution that describes some event or process and the integration is over the support of the PDF. The mean of the probability distribution (also referred to as the first moment about the origin) is

$$(2.5) \quad \bar{\xi} = \mathbb{E}[\xi] = \int \xi p(\xi)d\xi.$$

The  $r^{th}$  moment about the mean is given by

$$(2.6) \quad \mathbb{E}[(\xi - \bar{\xi})^r] = \int (\xi - \bar{\xi})^r p(\xi)d\xi.$$

The variance, skewness, and kurtosis are related to the  $2^{nd}$ ,  $3^{rd}$ , and  $4^{th}$  moments about the mean. In some cases, the integrals can be evaluated analytically, in others, the integrals are replaced by discrete sums. In the application problems to follow, we sampled from a Normal (Gaussian) distribution with a mean  $\mu$  and standard deviation  $\sigma$ . The probability density function (PDF) of the Normal distribution,  $p_N(\xi)$ , also denoted  $N[\mu, \sigma]$ , is given by:

$$(2.7) \quad p_N(\xi) = \frac{e^{-\frac{(\xi-\mu)^2}{2\sigma^2}}}{\sqrt{2\pi}\sigma}.$$

Two typical samples are shown in Figure 2.1 in which the Gaussian shape of the underlying PDF is evident. Frequently, it is convenient to use the standard normal variable,  $N[0, 1]$ , i.e., a Gaussian with a mean of 0 and a variance of 1, its definition follows directly from Eq. (2.7).

The Monte Carlo method has the property that it converges to the exact stochastic solution as the number of samples,  $n \rightarrow \infty$ . However, convergence of the mean error estimate is relatively slow since the standard deviation of the mean scales inversely with the square root of the the number of samples,

$$(2.8) \quad \sigma_u = \frac{\sigma}{\sqrt{n}}$$

Substantial efficiency improvements over the basic scheme, known as variance reduction techniques, are reported in the literature (see e.g. [22], [24], [25], [32]). The two primary mechanisms for improving the basic procedure are importance sampling and correlation methods.

**2.4. Moment Methods.** A number of applications using moment methods have appeared in the literature involving CFD simulations (see [26], [27], [28], [37], [44]). Moment method approximations are obtained from truncated Taylor series expansions about the expected value of the input parameter. For example, consider a function,  $u(\xi)$ , expanded about the mean value,  $\bar{\xi}$ . The first-order accurate approximation for the expected value of  $u$ , is:

$$(2.9) \quad \mathbb{E}_{FO}[u(\xi)] = u(\bar{\xi}).$$

Note that the first-order first moment (FOFM) approximation is nothing more than the pointwise (or deterministic) value evaluated at the mean of the input. Frequently, this is referred to as the deterministic solution. The second-order first moment (SOFM) requires the computation of the second (sensitivity) derivative to improve the estimate of the mean,

$$(2.10) \quad \mathbb{E}_{SO}[u(\xi)] = u(\bar{\xi}) + \frac{1}{2} \text{Var}(\xi) \left. \frac{\partial^2 u}{\partial \xi^2} \right|_{\bar{\xi}}.$$

For some problems we investigated, the improvement due to the higher order correction term was significant whereas for other problems it was not. Estimates of the variance are obtained similarly. The first order approximation to the variance of  $u$  is:

$$(2.11) \quad \text{Var}_{FO}[u(\xi)] = \left( \left. \frac{\partial u}{\partial \xi} \right|_{\bar{\xi}} \right)^2 \text{Var}(\xi).$$

The second order estimate of the variance of  $u$  is:

$$(2.12) \quad \text{Var}_{SO}[u(\xi)] = \left( \left. \frac{\partial u}{\partial \xi} \right|_{\bar{\xi}} \right)^2 \text{Var}(\xi) + \frac{1}{2} \left( \left. \frac{\partial^2 u}{\partial \xi^2} \right|_{\bar{\xi}} \text{Var}(\xi) \right)^2.$$

For discussion purposes, we shall refer to these first- and second-order approximations to the second moment as FOSM, SOSM methods respectively. Extension to multiple random variables is straightforward through Taylor series expansions of functions involving multiple variables. For example, if  $u = u(\xi_1, \xi_2)$ , the first-order moment approximations to the expected value and variance respectively are

$$(2.13) \quad \mathbb{E}_{FO}[u(\xi_1, \xi_2)] = u(\bar{\xi}_1, \bar{\xi}_2),$$

$$(2.14) \quad \text{Var}_{FO}[u(\xi_1, \xi_2)] = \left( \left. \frac{\partial u}{\partial \xi_1} \right|_{\bar{\xi}} \right)^2 \sigma_{\xi_1}^2 + \left( \left. \frac{\partial u}{\partial \xi_2} \right|_{\bar{\xi}} \right)^2 \sigma_{\xi_2}^2 + 2 \left( \left. \frac{\partial u}{\partial \xi_1} \right|_{\bar{\xi}} \right) \left( \left. \frac{\partial u}{\partial \xi_2} \right|_{\bar{\xi}} \right) \text{Covar}(\xi_1, \xi_2),$$

where the covariance (a measure to the extent that  $\xi_1$  and  $\xi_2$  vary jointly) between the random variables  $\xi_1$  and  $\xi_2$  can be defined in terms of expected values as

$$(2.15) \quad \text{Covar}(\xi_1, \xi_2) = \mathbb{E}[\xi_1 \xi_2 - \mathbb{E}(\xi_1) \mathbb{E}(\xi_2)].$$

TABLE 2.2  
Quantiles of the Standard Normal Distribution.

$\alpha$ (%)	Quantile( $\frac{1+\alpha}{2}$ )
67.000	0.97
90.000	1.64
95.000	1.96
99.000	2.58
99.900	3.29
99.990	3.89
99.999	4.42

Frequently, it is useful to define and use the correlation coefficient,

$$\rho_{\xi_1, \xi_2} \equiv \frac{\text{Covar}(\xi_1, \xi_2)}{\sigma_{\xi_1} \sigma_{\xi_2}} \in [-1, 1].$$

The extension of Eq.(2.14) to  $n$  independent random variables with standard deviations  $(\sigma_{\xi_1}, \dots, \sigma_{\xi_n})$  results in the standard error estimate for  $\sigma_u$ ,

$$(2.16) \quad \sigma_u = \left[ \sum_{i=1}^n \left( \frac{\partial u}{\partial \xi_i} \right)^2 \sigma_{\xi_i}^2 \right]^{\frac{1}{2}}.$$

Note the similarity of this FOSM estimate assuming uncorrelated data with the propagation of error formula, Eq.(2.3). In a probabilistic approach, one commonly uses an input uncertainty with a specified confidence interval, e.g.  $\bar{T} \pm 1.96\sigma_{\bar{T}}$ , a 95% mean confidence interval. Recall that a confidence interval gives a bound within which a parameter is expected to lie with a certain probability. It is common practice to distinguish between single prediction confidence intervals in which a randomly drawn, individual (i.e., single) sample is expected to lie with a pre-specified probability and mean confidence intervals in which the population mean is expected to be contained, again with a prescribed probability. Confidence intervals can be obtained from knowledge of the quantiles of the distribution. A quantile is a measure of the location of a point such that a specified fraction of the data lies to its left. For example, the median is the quantile measuring the location of the point such that 50% of the data lie to its left. Quantiles of the standard normal distribution for various confidence intervals are shown in Table 2.2. The important difference between the interval estimate Eq.(2.3) used by Turgeon and the probabilistic approach, Eq.(2.16), is the interpretation of the input uncertainty and hence *the scale factor* for the sensitivity derivatives. Note that  $\pm 3$  standard deviations contains more than 99% of the interval and  $\pm 4$  standard deviations contains 99.99% of the interval. If experimental data is available, then estimates of the input standard deviations,  $\sigma_{\xi_i}$ , can be obtained that will be less (and possibly substantially less) than the width of the uncertainty interval,  $\Delta\xi_i$ , used in Eq.(2.3). This distinction is further highlighted in Section 4 for a non-linear convection-diffusion problem. Certainly, repeated experimental measurements will give rise to a probability density function that describes the statistics of the distribution which can then be used to generate accurate and reliable probabilistic output for multi-disciplinary risk-based design activities.

**2.5. Polynomial Chaos.** Recently, several papers have appeared in the literature investigating spectral representations of uncertainty (see [14], [15], [16], [17], [47], [48]). An important concept of this approach is

the decomposition of a random function (or variable) into separable deterministic and stochastic components. Specifically, for a velocity field with random fluctuations, we write,

$$(2.17) \quad u(x, \xi) = \sum_{i=0}^P u_i(x) \Psi_i(\xi)$$

where  $u_i(x)$  is the deterministic part and  $\Psi_i(\xi)$  is the random basis function corresponding to the  $i^{th}$  mode. Effectively,  $u_i(x)$  is the amplitude of the  $i^{th}$  fluctuation. The discrete sum is taken over the number of modes represented,  $P = \frac{(n+p)!}{n!p!}$ , which is a function of the order of the polynomial chaos,  $p$ , and the number of random dimensions,  $n$ . Here, we use multi-dimensional Hermite polynomial basis functions to span the  $n$ -dimensional random space that we wish to represent although the use of many other basis functions are possible. A convenient form of the Hermite polynomials is given by

$$(2.18) \quad H_n(\xi_{i_1}, \dots, \xi_{i_n}) = e^{\frac{1}{2}\xi^T \xi} (-1)^n \frac{\partial^n}{\partial \xi_{i_1} \dots \partial \xi_{i_n}} e^{-\frac{1}{2}\xi^T \xi},$$

where  $\xi = (\xi_{i_1}, \dots, \xi_{i_n})$  is the  $n$ -dimensional random variable vector. As discussed in [47], there is a one-to-one correspondence between the functions  $H_n(\xi_{i_1}, \dots, \xi_{i_n})$  and  $\Psi_i(\xi)$ . The Hermite polynomials form a complete orthogonal set of basis functions in the random space. In terms of the inner product,

$$(2.19) \quad \langle f(\xi)g(\xi) \rangle = \int_{-\infty}^{\infty} f(\xi)g(\xi)W(\xi)d\xi$$

with the weight function  $W(\xi)$  taking the form of an  $n$ -dimensional Gaussian distribution with unit variance defined by

$$(2.20) \quad W(\xi) = \frac{1}{\sqrt{(2\pi)^n}} e^{-\frac{1}{2}\xi^T \xi},$$

the inner product of the basis functions is zero with respect to each other, i.e.,

$$(2.21) \quad \langle \Psi_i \Psi_j \rangle = \langle \Psi_i^2 \rangle \delta_{ij},$$

where  $\delta_{ij}$  is the Kronecker delta function. Once the modes,  $u_k$ , of the solution are known, then statistics of the distribution can be readily evaluated. The mean of the random solution is given by  $\mathbb{E}_{PC}[u] = u_0$ . The  $k = 1, \dots, n$  modes are the Gaussian estimates of the variance, all higher modes provide non-Gaussian interactions. The variance of the distribution is given by

$$(2.22) \quad \text{Var}_{PC}[u] = \sum_{i=1}^P [u_i^2(x) \langle \Psi_i^2 \rangle].$$

**3. Linear Convection with a Source Term.** The primary focus of this example is on the application of interval analysis for both time-dependent and steady-state calculations. We consider the scalar wave equation with a source term designed to mimic chemically-reacting flow problems in which  $\tau$  plays the role of a chemical time scale,  $\tau \rightarrow 1/k_f$ , where  $k_f$  is the forward reaction rate. The governing equation is

$$(3.1) \quad \frac{\partial u}{\partial t} + a \frac{\partial u}{\partial x} = -\frac{u}{\tau},$$

in which  $a$  is the convective wave speed (taken to be  $a = 1$  for all cases considered). Near chemical equilibrium, reaction rates are essentially instantaneous, i.e.,  $k_f \rightarrow \infty$  and  $\tau \rightarrow 0$ , resulting in disparate time scales that cause numerical “stiffness”. This problem has been studied by Godfrey [18] in connection

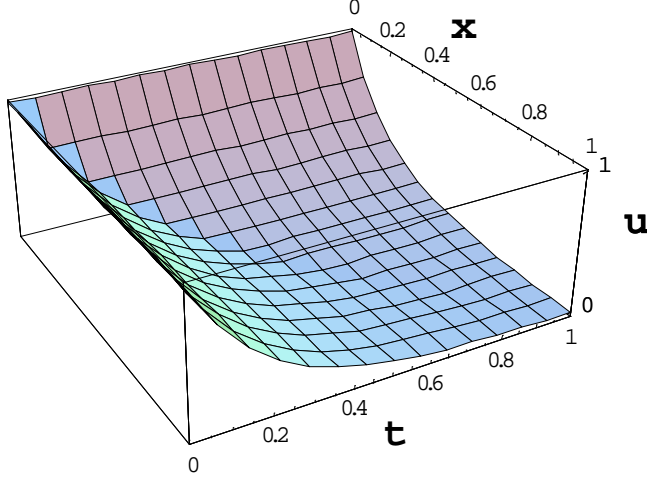


FIG. 3.1. *Exact time-dependent solution to the model problem.*

with implicit preconditioning algorithms. Here, we consider uncertainty in the chemical time scale,  $\tau$ , due to uncertainty in measured reaction rates. The exact solution to this equation is

$$(3.2) \quad u(x, t) = g\left(t - \frac{x}{a}, \tau\right) e^{-x/a\tau}.$$

In order to complete the definition of this problem, the initial and boundary condition, respectively, are taken to be

$$(3.3) \quad u(x, 0) = 1 \quad x \in [0, 1],$$

$$(3.4) \quad u(0, t) = 1 \quad \forall t > 0.$$

With these conditions, the function,  $g$ , is

$$(3.5) \quad g\left(t - \frac{x}{a}, \tau\right) = \begin{cases} 1, & t \geq \frac{x}{a} \\ e^{-(t-x/a)/\tau}, & 0 \leq t < \frac{x}{a}. \end{cases}$$

Taking the chemical time scale,  $\tau = 0.2$ , and the wave speed,  $a = 1$ , a graph of the exact deterministic time-dependent solution from  $t = 0$  to  $t = 1$  is shown in Figure 3.1. For the uncertainty analysis, we will examine the time-dependent behavior at  $x = 1$  (seen along the front side) and the steady state solution (seen along the right edge).

**3.1. Interval Analysis.** First-order upwind differences were used to approximate the spatial derivative in Eq. (3.1). The outflow boundary condition ( $x = 1$ ) was prescribed by approximating  $\frac{\partial u}{\partial x}|_{x=1} = 0$  to first order accuracy. Three time integration methods were implemented: Euler explicit, Euler implicit, and 4-stage Runge-Kutta. In terms of the steady-state residual,  $R(u) \equiv a \frac{\partial u}{\partial x} + \frac{u}{\tau}$ , the Euler explicit method for  $u_t + R(u) = 0$  can be written as:

$$(3.6) \quad u^{(n+1)} = u^{(n)} - \Delta t R(u^{(n)}) \quad (\text{Euler Explicit-1}).$$

For a deterministic problem, that is all there is to this method (referred to hereafter as Euler Explicit - 1). However, consider the case in which there is uncertainty in the input chemical time scale,  $\tau$ . Let  $\tau$  be defined to be the interval

$$(3.7) \quad \tau \equiv \bar{\tau}[1 - \varepsilon, 1 + \varepsilon],$$

where  $\bar{\tau}$  is the midpoint of the interval with uncertainty  $\varepsilon$ . The residual in Eq.(3.6) is now an interval rather than a point value at any  $x$  location. Moreover,  $u^{(n)}$  is also an interval after the first iteration as a consequence of interval operations during the previous time step even if the initial condition has no uncertainty. As seen in Figure 3.2, this method results in exponential growth of the intervals during a time accurate simulation. One can consider alternatives, namely,

$$(3.8) \quad u^{(n+1)} = u^{(n)} - \Delta t R(\bar{u}^{(n)}) \quad (\text{Euler Explicit-2})$$

$$(3.9) \quad u^{(n+1)} = \bar{u}^{(n)} - \Delta t R(u^{(n)}) \quad (\text{Euler Explicit-3})$$

$$(3.10) \quad u^{(n+1)} = \bar{u}^{(n)} - \Delta t R(\bar{u}^{(n)}) \quad (\text{Euler Explicit-4}).$$

where  $\bar{u}$  is the midpoint of the interval. Methods 2 and 4 evaluate the residual with the midpoint of the interval from the previous time step. However,  $R(\bar{u}^{(n)})$  is still an interval since the chemical time scale is uncertain. Since Method 4 also uses the midpoint value in the time derivative, it gives only the *local* uncertainty at each step due strictly to the uncertainty in  $\tau$ . For this problem, this results in very small interval estimates in which the upper and lower interval bounds visually appear to be on top of one another. Method 2 uses the interval  $u^{(n)}$  in the time derivative and hence accounts for cumulative growth. In fact, at any point in time, the cumulative (integrated) sum to time  $t$  of the uncertainty from Method 4 is equivalent to the Method 2 uncertainty at time  $t$ . Methods 1 and 3 both use the interval  $u^{(n)}$  to evaluate the residual and hence allow for temporal growth of uncertainty. The magnitude of the output intervals will grow without bound in Method 1 and yet with Method 3 converge to steady-state values (provided a steady-state exists). The results of these four methods with 81 equally-spaced grid points along the  $x$  - *axis* and using a time step  $\Delta t$  corresponding to  $\lambda \equiv \frac{a\Delta t}{\Delta x} = \frac{1}{2}$ , are shown in Figure 3.2.

It is common practice to monitor the convergence of a solution process in CFD simulations in terms of a vector norm of the steady-state residual,  $R(u^{(n)})$ . In this case, however,  $R(u^{(n)})$  is an interval not suitable for obtaining point-wise vector norm values hence we monitored the  $L_2$  - *norm* of  $R(\bar{u}^{(n)})$ . The residual histories of the four methods are shown in Figure 3.3. For Method 1, the interval size rapidly reaches the maximum machine representation, on this computer  $\{-1.79769 \times 10^{308}, 1.79769 \times 10^{308}\}$  which results in a midpoint residual of zero although the solution is completely useless. The other three methods smoothly converge to the steady-state in  $t < 2$  yet the exact steady-state is achieved at  $t = 1$ . However, in all cases, the residuals at  $t = 1$  have been reduced more than three orders of magnitude and the values at this time are close to their steady-state values.

One of the most common 4-stage Runge-Kutta methods (and the one implemented) can be written as

$$(3.11) \quad \begin{aligned} \gamma_1 &= R(u^{(n)}), \\ \gamma_2 &= R(u^{(n)} + \gamma_1/2), \\ \gamma_3 &= R(u^{(n)} + \gamma_2/2), \\ \gamma_4 &= R(u^{(n)} + \gamma_3), \\ \Delta u^{(n)} &= -\frac{\Delta t}{6}(\gamma_1 + 2\gamma_2 + 2\gamma_3 + \gamma_4), \\ u^{(n+1)} &= u^{(n)} + \Delta u^{(n)}. \end{aligned}$$

Again, we face the same issues as before, namely the residual evaluation,  $R(u)$  vs  $R(\bar{u})$ , and the update step,  $u^{(n)}$  vs  $\bar{u}^{(n)}$ . Numerical experiments confirm that the use of  $R(\bar{u})$  for the residual evaluations and  $u^{(n)}$  in the update step yields the most useful interval analysis results.

For many CFD simulations, implicit time integration methods are preferred. For demonstration pur-

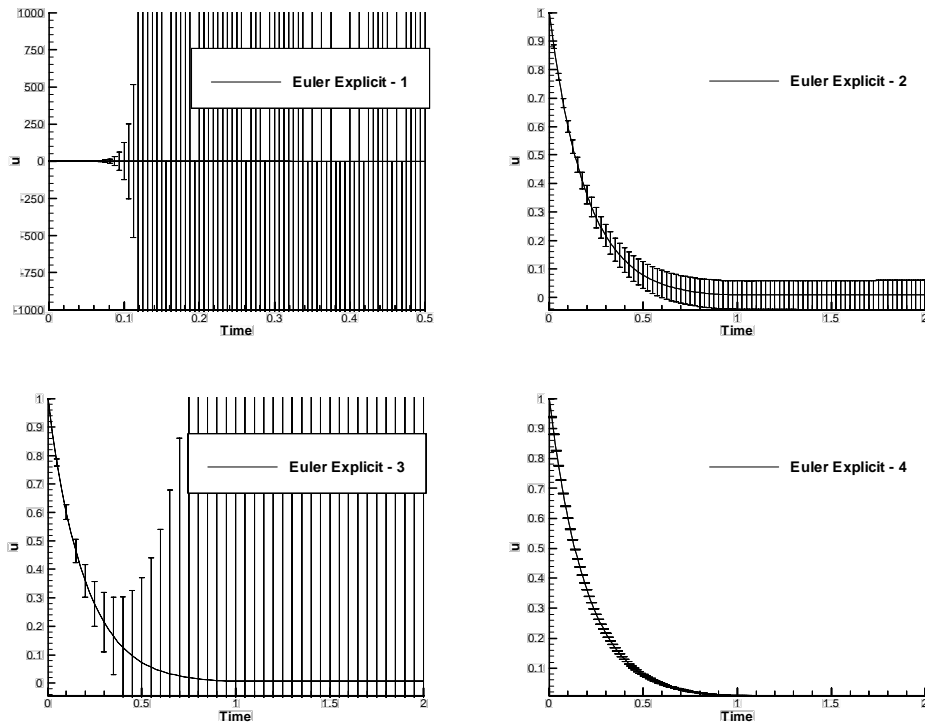


FIG. 3.2. Interval analysis results using different variations on the Euler Explicit method.

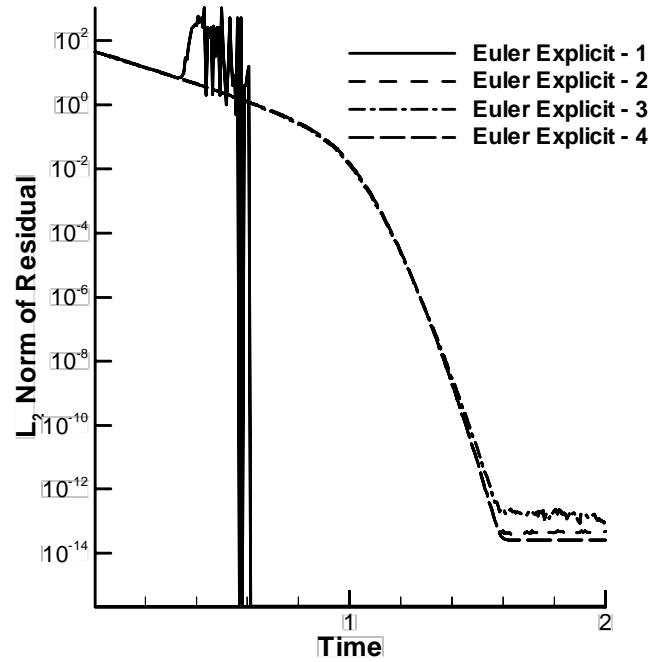


FIG. 3.3. Convergence histories for the four implementations of the Euler Explicit method for interval analysis.



poses, we implemented the Euler implicit time integration scheme which in delta form can be written as

$$(3.12) \quad \left( \frac{1}{\Delta t} + \frac{\partial R}{\partial u} \right)^{(n)} \Delta u^{(n)} = -R(u^{(n)}),$$

$$u^{(n+1)} = u^{(n)} + \Delta u^{(n)}.$$

This results in the tri-diagonal set of equations

$$(3.13) \quad \begin{bmatrix} b_1 & c_1 & & & & \\ a_2 & b_2 & c_2 & & & \\ & & & \ddots & & \\ & & & & a_{n-1} & b_{n-1} & c_{n-1} \\ & 0 & & & a_n & b_n & \\ & & & & & & \end{bmatrix} \begin{Bmatrix} \Delta u_1 \\ \Delta u_2 \\ \vdots \\ \Delta u_{n-1} \\ \Delta u_n \end{Bmatrix} = - \begin{Bmatrix} R(u_1) \\ R(u_2) \\ \vdots \\ R(u_{n-1}) \\ R(u_n) \end{Bmatrix}$$

where for the general case of wave speeds of either sign,

$$(3.14) \quad \left. \begin{aligned} a_j &= -\frac{a+|a|}{2\Delta x} \\ b_j &= \frac{1}{\Delta t} + \frac{1}{\tau} + \frac{|a|}{\Delta x} \\ c_j &= \frac{a-|a|}{2\Delta x} \end{aligned} \right\} \quad j = 2, \dots, n-1.$$

At the inflow boundary,  $c_1 = R(u_1) = 0$  and  $b_1 = 1$  and at the outflow,  $a_n = -1, b_n = 1, R(u_n) = 0$ . For positive wave speeds, the above matrix reduces to a lower bi-diagonal matrix which can be solved by a forward substitution pass. Likewise, for negative wave speeds, the matrix (with appropriate change in boundary conditions) reduces to an upper bi-diagonal matrix which can be solved by a backward substitution step.

Using the interval midpoint for residual evaluations, a comparison of the time history from the Euler explicit, Euler implicit, and 4-stage Runge-Kutta methods at  $x = 1$  is shown in Figure 3.4. Although difficult to see, the Euler implicit and Euler explicit methods yield identical results in terms of interval size. The Runge-Kutta method results in larger intervals due to the increased number of residual evaluations and intermediate update steps in the multi-step method.

If one is only interested in the steady-state solution, other options become available, primarily through the use of algorithms that are stable for large time steps and in some cases, space-marching methods. In this case, both are applicable. For example, the Euler implicit method, Eq. (3.12) can be used with  $\Delta t \rightarrow \infty$ . Since the governing equation is linear, the steady solution is obtained in one step by solving the resulting linear problem which we refer to as a Time March method. The other alternative is to implement a Space March method by eliminating the time derivative in Eq. (3.1), i.e.,

$$(3.15) \quad a \frac{\partial u}{\partial x} = -\frac{u}{\tau}.$$

Discretizing this equation with first-order upwind differences (taking  $a > 0$ ) yields

$$(3.16) \quad u_j = \frac{u_{j-1}}{1 + \frac{\Delta x}{a\tau}}$$

where  $u_j \equiv u(j\Delta x)$ . The results of the Time March versus Space March approaches can be seen in Figure 3.5 where the advantage of space marching is evident.

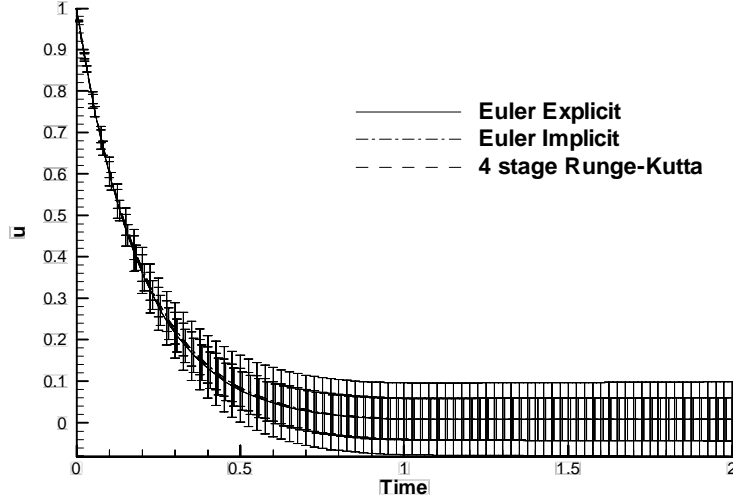


FIG. 3.4. Time accurate interval calculations with Euler explicit, Runge-Kutta, and Euler implicit time integration methods.

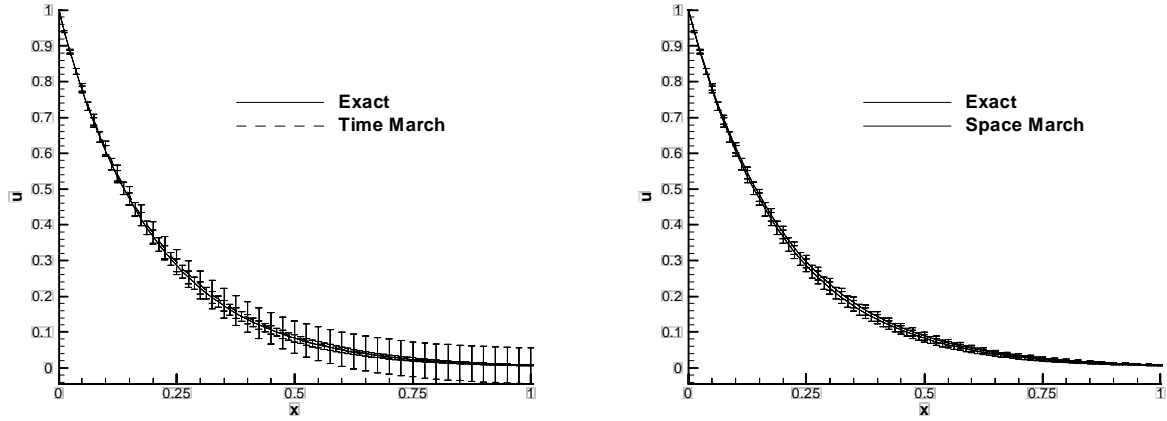


FIG. 3.5. Steady state interval solution using the Euler implicit method with an infinite time step (Time March) compared to a space-marching method.

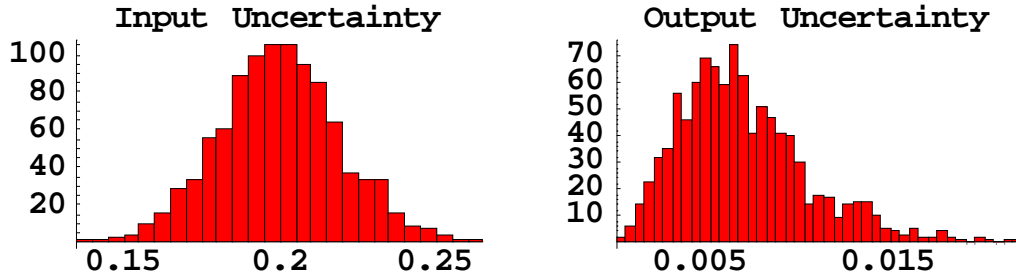


FIG. 3.6. Histograms of the input chemical time scale,  $\tau$ , and the output variable,  $u$  at  $x = 1$  from 1000 Monte Carlo simulations.

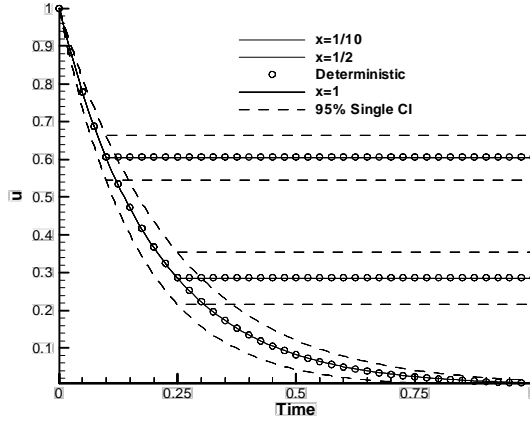


FIG. 3.7. Mean values and 95% single prediction confidence intervals from time-dependent Monte Carlo at three  $x$  locations.

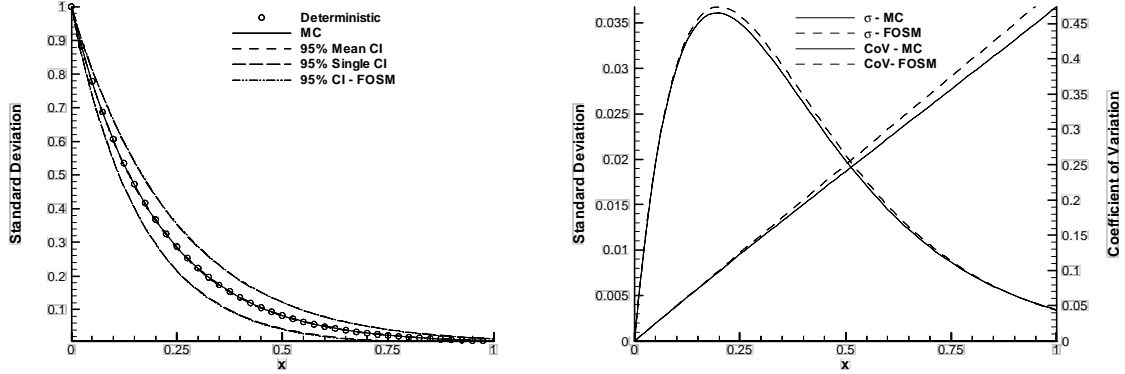


FIG. 3.8. Comparison of the First-Order Moment method with 1000 Monte Carlo simulations.

**3.2. Monte Carlo and Moment Method.** The Monte Carlo and First-Order moment methods were also implemented. For these probabilistic methods, we took the chemical time scale,  $\tau$ , to be a Gaussian random variable with a mean,  $\bar{\tau} = 0.2$  and a 5% coefficient of variation (CoV). Figure 3.6 shows histograms from 1000 Monte Carlo simulations where it can be seen that the output is clearly non-Gaussian.

Time-dependent Monte Carlo calculations are compared at three  $x$  locations in Figure 3.7. For this problem, the solution at any  $x$  decays from the initial condition of  $u = 1$  until its steady-state value is reached at  $t = \frac{x}{a}$ . The 95% mean confidence intervals are roughly 30 times narrower and are not shown here for clarity. Steady-state results from the FO moment method are compared with 1000 Monte Carlo simulations in Figure 3.8. The sensitivity derivative required to implement the FO moment method is

$$(3.17) \quad \frac{\partial u}{\partial \tau} = \frac{x}{a\tau^2} e^{-x/a\tau}.$$

The 95% confidence intervals from the FOSM are comparable to the single prediction 95% confidence intervals from Monte Carlo. The distribution of standard deviation and coefficient of variation are in good overall agreement.

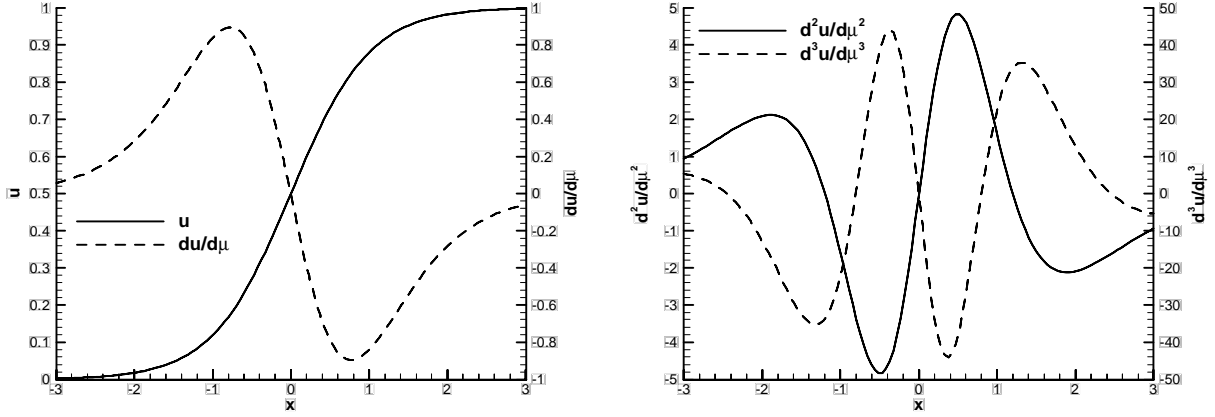


FIG. 4.1. *Exact deterministic solution and first three sensitivity derivatives.*

**4. Non-linear Burgers Equation.** Computational fluid dynamicists frequently study simplified problems designed to mimic certain features of a more complicated situation but at lower cost and effort. Many such problems exist but one that is particularly useful is the model non-linear convection-diffusion problem proposed by Rakich and referred to as the general Burgers equation [4]. Based on specific choices of parameters in the equation, one can obtain linear or non-linear behavior. We consider the steady form of this equation, which in conservation law form is

$$(4.1) \quad \frac{\partial f}{\partial x} - \frac{\partial}{\partial x} \left( \mu \frac{\partial u}{\partial x} \right) \equiv R(u) = 0$$

where the flux,  $f$ , is a non-linear function of  $u$ . We took the specific case of  $f = u \left( \frac{1}{2} - u \right)$  for which the exact stationary solution is given by

$$(4.2) \quad u(x) = \frac{1}{2} \left[ 1 + \tanh \left( \frac{x}{4\mu} \right) \right].$$

For the uncertainty analysis, we took the input viscosity to be stochastic, hence the sensitivity derivatives,  $\partial^n u / \partial \mu^n$ , are important in the analysis. The exact solution,  $u(x)$ , and its first three derivatives with respect to viscosity,  $\mu$ , are shown in Figure (4.1). The solution rises monotonically from 0 at  $-\infty$  to 1 at  $+\infty$ . Note that the higher derivatives are increasingly oscillatory. One practical consequence of this that we found was the need for high-order methods or finer grids to numerically estimate those derivatives.

For all numerical computations, we limited the computational domain to  $x \in [-3, 3]$ . Truncating infinite domains in CFD is commonplace, external flow over airfoils, wings, and aircraft configurations are a few examples. However, there are consequences of this with regard to boundary condition treatment of stochastic variables. A more complete discussion of this topic and a random field analysis of this problem can be found in [29].

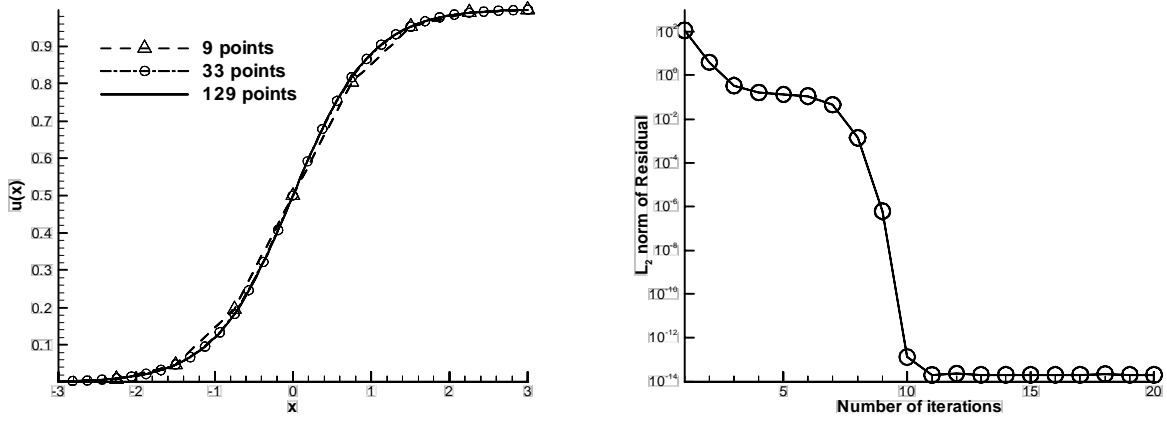


FIG. 4.2. Numerical solutions using a second-order accurate centered scheme on three mesh levels(left). Typical convergence history using Newton's method for the general Burger equation (right).

**4.1. Deterministic Problem.** Newton's method was used to solve the non-linear problem, Eq.(4.1). This results in the linearized system of equations and the update step

$$(4.3) \quad \left( \frac{\partial R}{\partial u} \right)^{(n)} \Delta u^{(n)} = -R(u^{(n)}),$$

$$u^{(n+1)} = u^{(n)} + \Delta u^{(n)}.$$

Second-order centered differences were used to approximate the spatial derivatives. Dirichlet boundary conditions were specified at the endpoints,  $x = \pm 3$ , from the exact deterministic solution. This results in a tri-diagonal set of equations to solve for each Newton iteration (for details, see [29])

$$(4.4) \quad \begin{bmatrix} b_1 & c_1 & & & & \\ a_2 & b_2 & c_2 & & & \\ & & & \ddots & & \\ & 0 & & & a_{n-1} & b_{n-1} & c_{n-1} \\ & & & & a_n & b_n & \end{bmatrix} \begin{Bmatrix} \Delta u_1 \\ \Delta u_2 \\ \vdots \\ \Delta u_{n-1} \\ \Delta u_n \end{Bmatrix} = - \begin{Bmatrix} R(u_1) \\ R(u_2) \\ \vdots \\ R(u_{n-1}) \\ R(u_n) \end{Bmatrix}$$

where

$$(4.5) \quad \begin{cases} a_j = -\frac{(1/2 - u_{j-1})}{2\Delta x} - \frac{\mu}{\Delta x^2} \\ b_j = \frac{2\mu}{\Delta x^2} \\ c_j = \frac{(1/2 - u_{j+1})}{2\Delta x} - \frac{\mu}{\Delta x^2}, \end{cases}$$

$b_1 = b_n = 1$ , and  $a_1 = c_1 = a_n = c_n = R(u_1) = R(u_n) = 0$ .

Numerical solutions were generated on a sequence of uniformly-spaced grids for which the number of grid points and mesh spacing is given in Table 4.1. The numerical solution for the dependent variable,  $u$ , on three different grids is shown in the left of Figure 4.2. A typical convergence history, corresponding to the 129 mesh point solution is on the right. Independent of the level of grid refinement, the residual converged to machine epsilon in the same number of iterations ( $\pm 1$ ).

Several approaches have been proposed for establishing truncation error estimates. Probably the most common approach is based on Richardson extrapolation although other estimates, such as multi-grid estimates

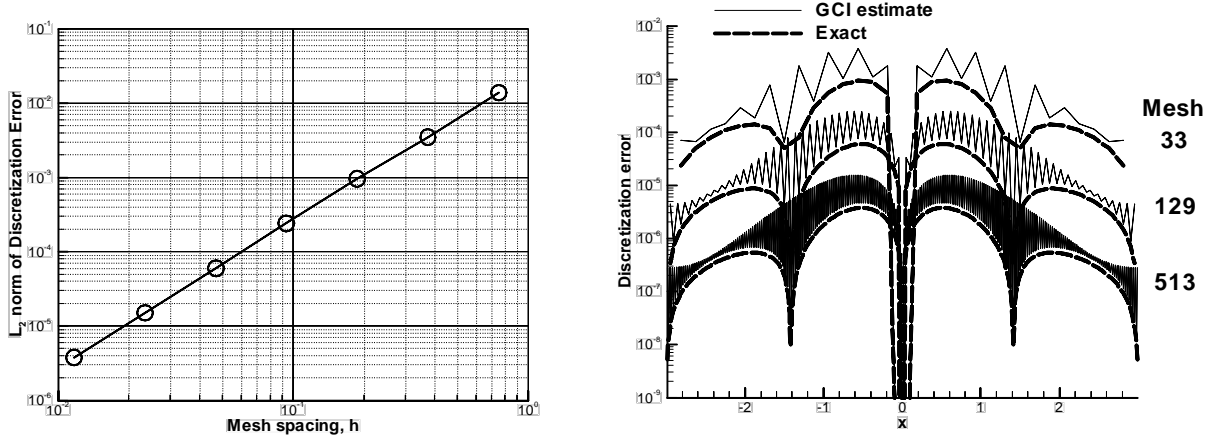


FIG. 4.3. Left - Convergence of the  $L_2$  error norm versus mesh spacing. Right - Distribution of exact and estimated discretization error on three grids.

can also be used. Roache [40] has used Richardson extrapolation with modifications to obtain an error estimator and this technique will be used here for demonstration purposes. The discretization error estimates that we require can be obtained by series expansions. The result is:

$$(4.6) \quad E_1 = \frac{\varepsilon}{1 - r^p} \quad \text{and} \quad E_2 = \frac{r^p \varepsilon}{1 - r^p}$$

where

$E_1, E_2 \equiv$  error estimates on the fine grid “1” and coarse grid “2”, respectively

$\varepsilon \equiv u_2 - u_1$ ; the pointwise difference between successive solutions

$r \equiv \frac{h_2}{h_1} > 1$ ; the ratio of mesh spacing

$p \equiv$  the order of accuracy of the numerical method.

The Grid Convergence Index ( $GCI$ ) used by Roache as a discretization error estimator is defined by

$$(4.7) \quad GCI \equiv F_s |E_1| \quad \text{or} \quad GCI \equiv F_s |E_2|$$

where  $F_s$  is a factor-of-safety with a recommended value of  $F_s = 1.25$  (which was used here) for high fidelity numerical experiments. In all cases examined, the  $GCI$  estimate bounded the true discretization error at every point in the domain. Note that error estimates are available on all grid levels. Roy [43] has extended this analysis to mixed-order schemes and further refinements are possible using information from additional grids.

Measures of accuracy and discretization error are shown in Figure 4.3. The plot on the left shows  $L_2$  – norm of the actual error. The slope of the line is well known to be a measure of the order of accuracy of the discretization. Table 4.1 shows the computed values of the slope of each line segment. The exact distribution of the discretization error is shown on the right of Figure 4.3 along with the Grid Convergence Index ( $GCI$ ) estimate.

TABLE 4.1  
Summary of grid convergence parameters and results for Burger’s equation.

Grid Level	Number of Grid Points	Mesh Spacing, $\Delta x$	$L_2$ -norm of Error	Slope of Segment
1	9	0.75	0.01383131	-
2	17	0.375	0.00350755	1.97940
3	33	0.1875	0.00095693	1.87398
4	65	0.09375	0.00023901	2.00129
5	129	0.046875	0.00006023	1.98851
6	257	0.0234375	0.00001505	2.00001
7	513	0.0117188	0.00000376	2.00000

## 4.2. Stochastic Problem.

**4.2.1. Exact Stochastic Solution.** The viscosity,  $\mu$ , was taken to be a Gaussian random variable,  $p_M(\mu)$ , with a mean  $\bar{\mu} = 0.25$  and a coefficient of variation,  $CoV(\mu) \equiv \frac{\sigma}{\mu} = 10\%$ . The exact stochastic solution can be expressed in terms of its probability density function, which is given by

$$(4.8) \quad p_U(u(x)) = \left| \frac{\partial}{\partial \mu} u(x, \mu) \right|^{-1} p_M(\mu).$$

Justification for this expression is rather intuitive since it is simply a statement that the probability of a random variable following within a specified range is constant under a transformation of variables. Using Eq.(4.1) and the definition of the Gaussian PDF, this expression can be analytically evaluated to obtain

$$(4.9) \quad p_U(u(x)) = \frac{e^{-\frac{\left(\frac{x}{4 \tanh^{-1}(1-2u)} + \bar{\mu}\right)^2}{2\sigma^2}}}{8\sqrt{2\pi}\sigma} \left| \frac{x}{(u-1)u \tanh^{-1}(1-2u)^2} \right|.$$

A plot of this function is shown in Figure 4.4 followed by the enlarged view in Figure 4.5 with more resolution of the PDF. It can be seen that  $p_U$  varies markedly with  $x$ . Near the boundaries, the PDF is highly skewed and peaked but approaches a Gaussian as  $x \rightarrow \pm 1$  from the nearest boundary. At  $x = 0$ , the solution is deterministic, i.e., the variance is zero, which all random variable models predict. As a side note, random field models may produce quite different results, particularly near the centerline [29].

**4.2.2. Interval Analysis.** We applied interval analysis to both the exact solution and the CFD-oriented numerical method described previously. The input interval object was the viscosity, which was defined to be

$$(4.10) \quad \mu = \bar{\mu}[1 - \varepsilon, 1 + \varepsilon].$$

Numerical results obtained by evaluating the exact deterministic solution, Eq. (4.2) for an input value,  $\varepsilon = 0.1$ , are shown in Figure 4.6. The error bars indicate the width of the output interval. One of the most attractive things about interval analysis is that it is very simple to implement. However, as seen in the interval analysis results from the numerical method in which both the Jacobian matrix and residual were evaluated with the interval midpoint values, Figure 4.7, the uncertainty estimates are unacceptably large. The bounds became so large for the bottom two cases that a change in scale was required to keep the error bars within the display area.

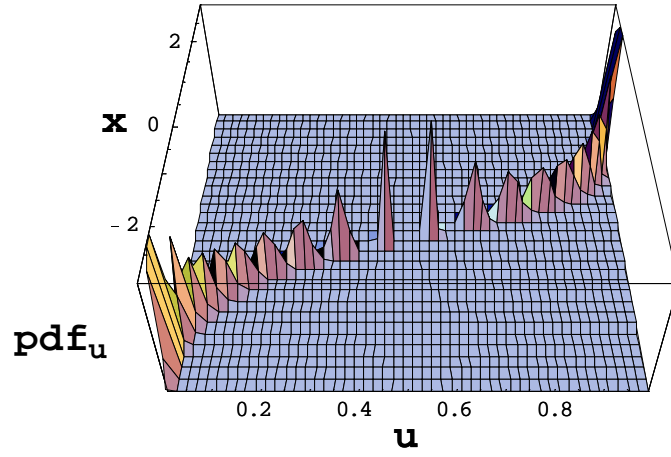


FIG. 4.4. Probability density function of the exact stochastic solution of the Burger equation.

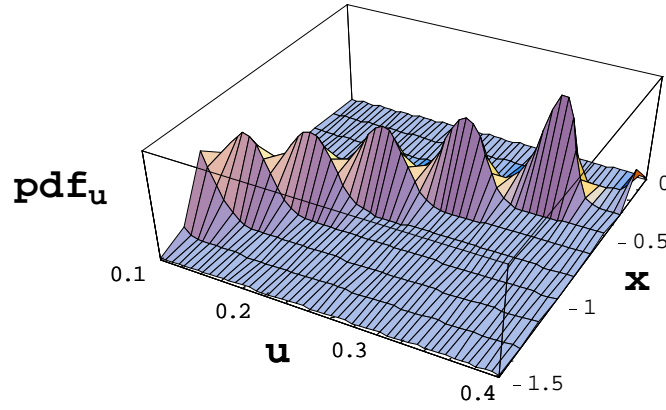


FIG. 4.5. Enlarged view of the exact probability density function of  $u$  for the Burger equation.

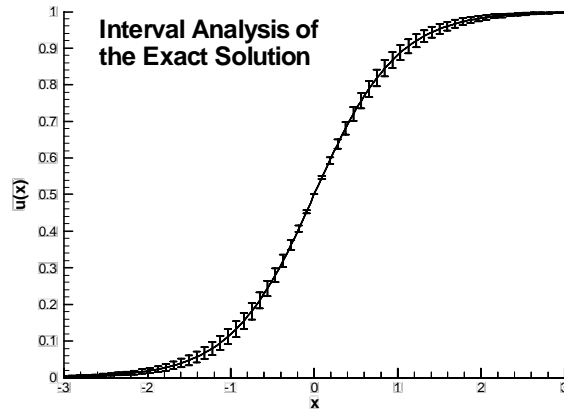


FIG. 4.6. Interval analysis of the exact deterministic solution for an input uncertainty in the viscosity,  $\epsilon = 0.1$  (i.e. 10%).



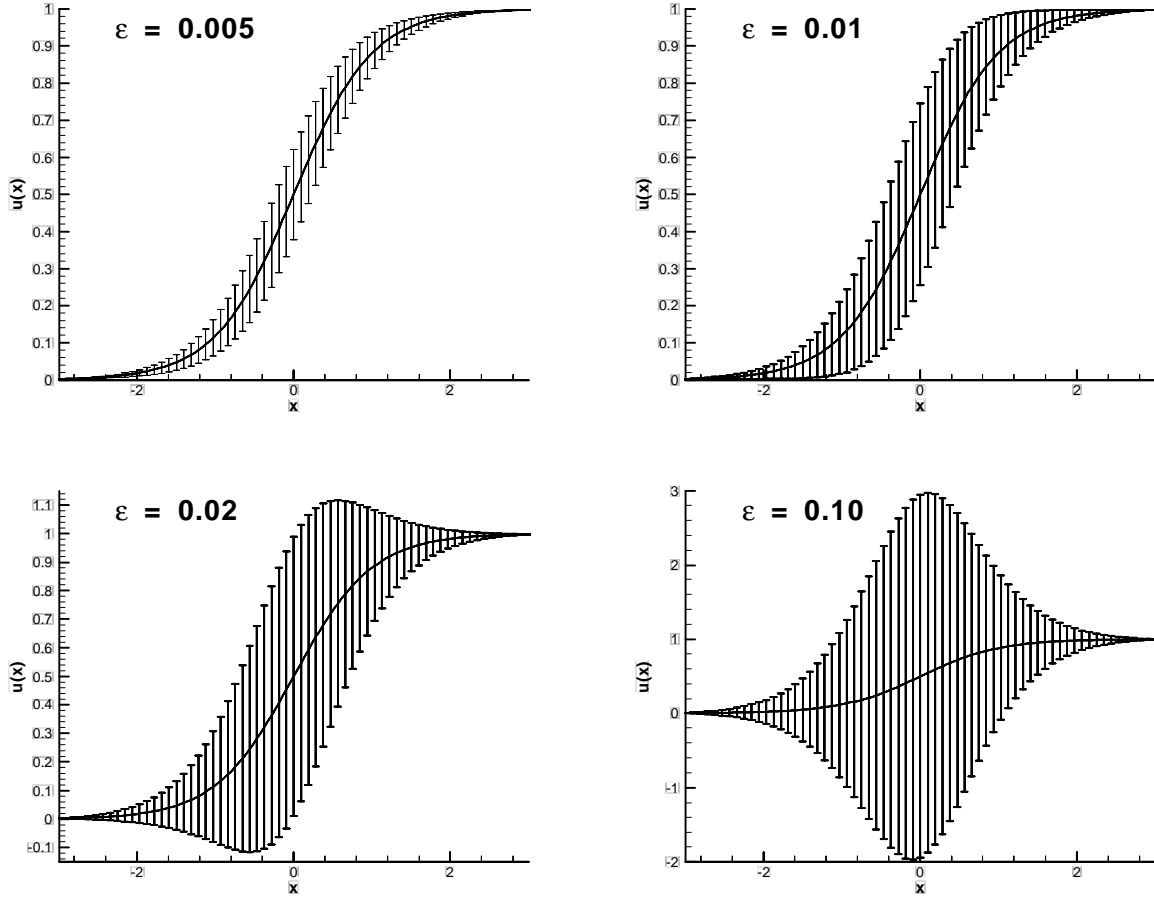


FIG. 4.7. Interval analysis results from the numerical solution of Burger's equation. Note the change in scale on the bottom two plots.

**4.2.3. Moment Methods.** The moment methods require the sensitivity derivatives with respect to the input random variable. In this example, we computed numerical approximations from the continuous sensitivity equation (CSE) approach and the discrete adjoint (DA) method. A brief description of these two techniques follows:

*Continuous Sensitivity Equation (CSE).* The conservation law form of the Burgers equation (4.1) can be re-written in quasi-linear form as

$$(4.11) \quad \lambda u_x = \mu u_{xx} \quad \text{where} \quad \lambda = \frac{1}{2} - u.$$

The continuous sensitivity equation is derived by differentiating Eq. (4.11) with respect to  $\mu$  noting that  $u = u(x; \mu)$ . Defining  $s_\mu \equiv \partial u / \partial \mu$  and carrying out the differentiation yields a linear differential equation for the sensitivity derivative, namely,

$$(4.12) \quad (\lambda s_\mu)_x = \mu (s_\mu)_{xx} + u_{xx}.$$

Given a numerical solution of the Burgers equation as input, one can use a variety of numerical methods to solve Eq. (4.12). We used a spatial discretization consistent with the flow solution method (i.e., a  $2^{nd}$  order

accurate centered scheme) and Newton's method. Since the problem is linear, one Newton iteration always finds the solution to machine precision ( $\approx 10^{-16}$ ). It is worth mentioning that the Jacobian matrix of the CSE equation is identical to the Jacobian matrix of the Burgers equation. This simplifies the coding of the CSE since one merely has to change the right hand side in the original software.

*Discrete Adjoint Method.* The discrete adjoint method is commonly used in aerodynamic optimization problems ([34]) in which a user defined cost function is minimized. The cost function, denoted  $F(u; \varsigma_i)$  where  $\varsigma_i$  represents the  $i^{th}$  generic design variable, is augmented with a vector of Lagrange multipliers operating on the discrete version of the governing equations, in this case Eq. (4.1), i.e.,

$$(4.13) \quad F^* = F(u; \varsigma_i) + \lambda^T R(u; \varsigma_i).$$

This equation is next differentiated with respect to the design variable, or more generally, any generic variable denoted  $\varsigma_i$ . After some rearrangement, one obtains

$$(4.14) \quad \frac{\partial F^*}{\partial \varsigma_i} = \left( \frac{\partial F}{\partial u} + \lambda^T \frac{\partial R}{\partial u} \right) \frac{\partial u}{\partial \varsigma_i} + \lambda^T \left( \frac{\partial R}{\partial \varsigma_i} \right)_u.$$

Since the vector of Lagrange multipliers is arbitrary, the first term in parentheses may be equated to zero to yield a linear system of equations for  $\lambda$ ,

$$(4.15) \quad \left( \frac{\partial R}{\partial u} \right)^T \lambda = - \frac{\partial F}{\partial u}.$$

Once the vector of Lagrange multipliers is known, the sensitivity of the cost function with respect to  $\varsigma_i$  can be evaluated from

$$(4.16) \quad \frac{\partial F}{\partial \varsigma_i} = \lambda^T \left( \frac{\partial R}{\partial \varsigma_i} \right)_u.$$

This basic implementation is widely used in a design environment (see [34]) and precludes the need to compute the flow sensitivities, i.e.,  $\partial u / \partial \varsigma_i$ , directly. In this problem, we require those derivatives and they can be readily obtained by defining the set of cost functions,  $F = \{F_j \equiv u_j | j = 1, 2, \dots, n\}$  where  $n$  is the total number of grid points. Extending Eq. (4.16) to a system of functions and inserting the definition of  $F$  yields

$$(4.17) \quad \left( \frac{\partial R}{\partial u} \right)^T \Lambda = -I$$

where  $I$  is the identity matrix and  $\Lambda$  is a matrix consisting of a set of column vectors,  $\lambda_j$  for each  $j$ . The required sensitivity derivatives can now be found from Eq. (4.14), which upon substitution and rearrangement reduces to

$$(4.18) \quad \frac{\partial u}{\partial \varsigma_i} = \Lambda^T \left( \frac{\partial R}{\partial \varsigma_i} \right)_u.$$

Note that Eq. (4.17) can be solved efficiently for all right hand sides by LU decomposition. All sensitivity derivatives can then be computed by the single matrix-vector multiply indicated in Eq. (4.18).

Although it may not be readily apparent, both the CSE and the DA methods yield identical results provided both methods are formulated and implemented consistently. In practice, this generally does not occur because of differences in coding, convergence level, etc. Here, however, the equations are always solved to machine precision, the discretizations are consistent, and consequently, the sensitivity derivatives obtained

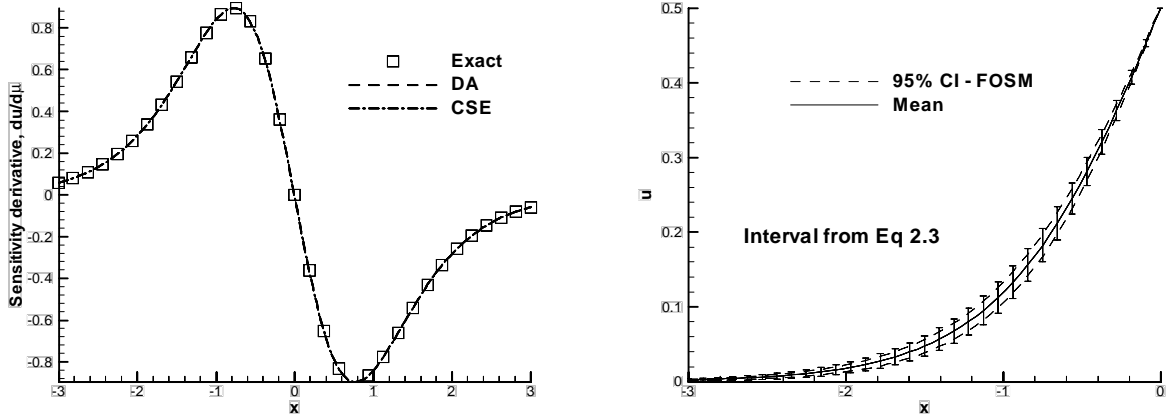


FIG. 4.8. Left - First sensitivity derivative computed by the discrete adjoint and continuous sensitivity methods compared to the exact solution. Right - Comparison of probabilistic (dashed lines) vs. non-probabilistic (error bars) interpretation of input uncertainty on  $x \in [-3, 0]$ .

by both methods are identical. A plot of the first derivative with respect to viscosity by both methods is shown on the left of Figure 4.8 and compared with the exact derivative. The right half of the figure shows results for estimating the uncertainty assuming that 1) the input uncertainty contains 100% of the error (non-probabilistic - Eq. (2.3)) and 2) a probabilistic FOSM approximation assuming that the input error represents three standard deviations ( $\approx 99\%$  of the samples). The advantage of knowledge about the input data is clearly seen in the reduced uncertainty in the output.

A comparison of the absolute error in the mean ( $\bar{\mu} = 0.25$ ) and relative error in the standard deviation ( $CoV(\mu) \equiv \frac{\sigma}{\mu} = 10\%$ ) predicted by Monte Carlo and the first- and second-moment methods are shown in Figure 4.9. The distribution of the mean error from the first-order moment method closely follows the second derivative distribution shown in Figure 4.1. Adding the second derivative correction term to obtain the second order moment estimate of the mean results in substantially less error. As can be seen on the right, the relative error in estimating the standard deviation is approximately 6% and 2% for the FOSM and SOSM estimates respectively at the boundaries. One thousand MC simulations results in roughly the same maximum error as the SOSM method at roughly 300 times the cost. Increasing the number of simulations an order of magnitude reduced the error by approximately three at considerable additional cost.

**4.2.4. Polynomial Chaos.** Substituting in polynomial chaos expansions for the dependent variable,  $u$ , and the input random variable,  $\mu$ , into the residual, Eq.(4.1), and taking the inner product,  $\langle \cdot, \Psi_k \rangle$  yields an equation for the residual of the  $k^{th}$  mode,

$$(4.19) \quad R_k = \frac{1}{2} \frac{\partial}{\partial x} \left[ u_k \langle \Psi_k^2 \rangle - \sum_{i=0}^P \sum_{j=0}^P e_{ijk} u_i u_j \right] - \sum_{i=0}^P \sum_{j=0}^P e_{ijk} \mu_i \frac{\partial^2 u_j}{\partial x^2}$$

where  $e_{ijk} \equiv \langle \Psi_i \Psi_j \Psi_k \rangle$ . We iteratively solved this equation by the Euler explicit method but found that the CPU time to achieve the machine zero steady-state solution was excessive relative to implicit methods. Consequently, Newton's method was implemented by using the linearization of the residual, which can be

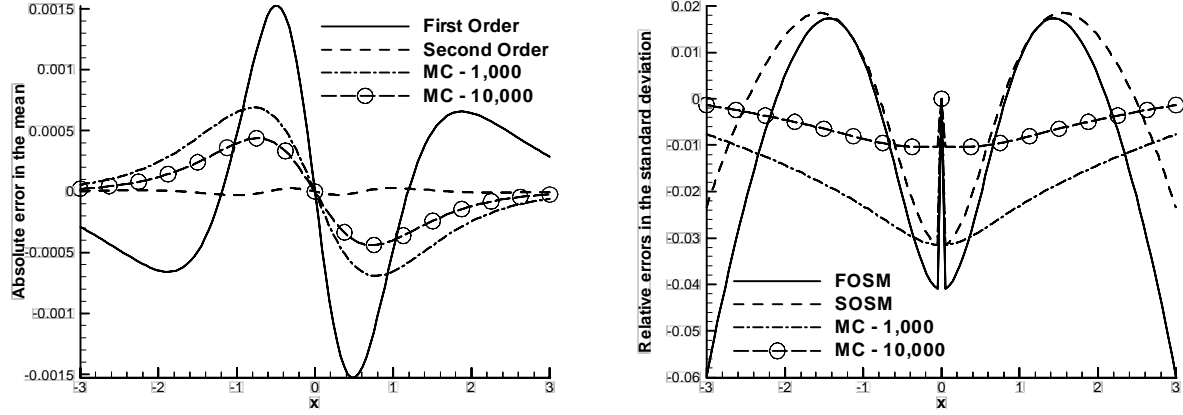


FIG. 4.9. Absolute error in the mean (left) and relative error in the standard deviation (right) using Monte Carlo and first- and second-moment methods.

shown to reduce to

$$(4.20) \quad \Delta R_k \simeq \frac{\partial R_k}{\partial u_l} \Delta u_l = \frac{1}{2} \frac{\partial}{\partial x} \left[ \left( \delta_{lk} \langle \psi_k^2 \rangle - \sum_{i=0}^P \sum_{j=0}^P e_{ijk} (u_i \delta_{lj} + u_j \delta_{li}) \right) \Delta u_l \right] - \sum_{i=0}^P \sum_{j=0}^P e_{ijk} \mu_i \frac{\partial^2 \Delta u_l}{\partial x^2}$$

where  $\delta_{lj}$  is the Kronecker delta function. The boundary conditions were specified from the exact stochastic solution by matching moments of the distribution up to a user-specified order. The three boundary conditions studied were obtained by matching

1. the mean (BC1)
2. the mean and variance (BC2)
3. the mean, variance, and skewness (BC3)

The first boundary condition, BC1, implies that the first mode,  $u_0$  is set to the mean of the exact solution and the remaining modes are set to zero on the boundary. The second boundary condition sets  $u_0$  and  $u_1$  to the mean and variance of the exact solution, respectively, the remaining modes are set to zero. Similarly, BC3 sets  $u_0$  to the mean and solves a simple algebraic problem to find the values of  $u_1$  and  $u_2$  such that the variance and skewness of the polynomial chaos distribution match the exact solution.

One advantage of Polynomial Chaos is that the output PDF's which depend on the order of the chaos can be easily obtained. For a single random variable, the first-order chaos yields a Gaussian distribution with mean  $u_0$  and standard deviation  $|u_1|$ , i.e.,

$$(4.21) \quad p_{PC_1}(u) = \frac{e^{-(u-u_0)^2/2u_1^2}}{\sqrt{2\pi}|u_1|}.$$

The higher-order modes account for non-Gaussian interactions and are reflected in the output PDF. For a second-order chaos, the result is

$$(4.22) \quad p_{PC_2}(u) = \frac{e^{-\left(u_1 + \sqrt{u_1^2 + 4u_2(u-u_0+u_2)}\right)^2/8u_2^2}}{\sqrt{2\pi|u_1^2 + 4u_2(u-u_0+u_2)|}}.$$

Further analytic representations for higher order chaoses are possible but lengthy.

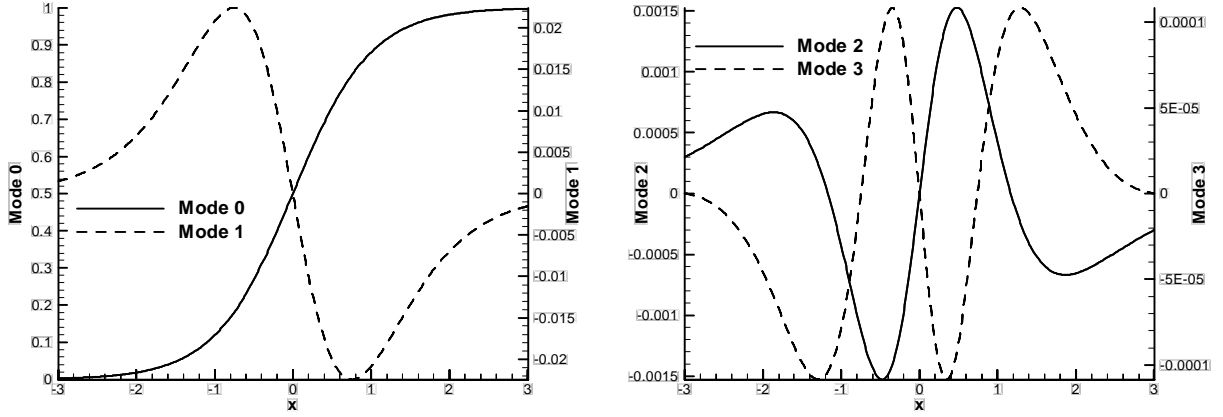


FIG. 4.10. The first four modes from Polynomial Chaos. Compare to the sensitivity derivatives of the exact solution.

Numerous results were generated using Hermite polynomial chaoses of varying order with different boundary condition treatment and on different grids. Here we summarize these results. The first four modes from an order 3 PC are shown in Figure 4.10. Recall that mode 0 represents the expected value (i.e., the mean). Note the similarity of the shapes of the higher modes with the sensitivity derivatives of the exact solution in Figure 4.1. The only discrepancy that can be seen is between the third mode and the third derivative which is due to boundary condition treatment for this mode and will be discussed subsequently.

Figure 4.11 shows absolute errors in the mean and relative errors in the standard deviation using order 1 and 2 PC on 129 and 513 point grids. Refining the grid for the first-order chaos gives a slightly larger maximum error than the coarser grid. Computations show that the first-order method is grid converged on the 129 point mesh, i.e., further grid refinement makes no appreciable reduction in error nor is there significant increases, just re-distribution. However, the second-order polynomial chaos is clearly not grid converged on the 129 point grid. There is a substantial reduction in the mean error on the finer 513 point grid. In terms of the estimates of the standard deviation, the first-order chaos results on both grids are similar and very close to the SOSM method (see Fig. 4.9). The 2<sup>nd</sup> order chaos has very small error in the standard deviation, almost an order-of-magnitude smaller than the estimate obtained from 10,000 Monte Carlo simulations.

A further examination of the error convergence versus the order of the PC was conducted. In theory, exponential reduction rate of the error as the order of the chaos is increased should be observed. In practical CFD simulations, there are issues that are likely to make such convergence rates unachievable although this does not preclude the use or utility of the polynomial chaos method. Figure 4.12 supports this statement where, on the left, the convergence behavior of the  $L_2$  norm shows that in order to achieve the “theoretical” convergence, more and more information needs to be supplied at the boundary as the order of the chaos increases (see Table 4.2). This simply means that in order to match the exact solution to a given level of accuracy, boundary conditions must also be specified consistent with the level of accuracy sought. Thus, to stay on the exponential convergence curve, higher order chaoses require higher order statistics at the boundaries of the computational domain. Note also that finer grids are also required to stay on the exponential reduction rate curve due to the increased frequency content inherent in the higher order modal solutions.

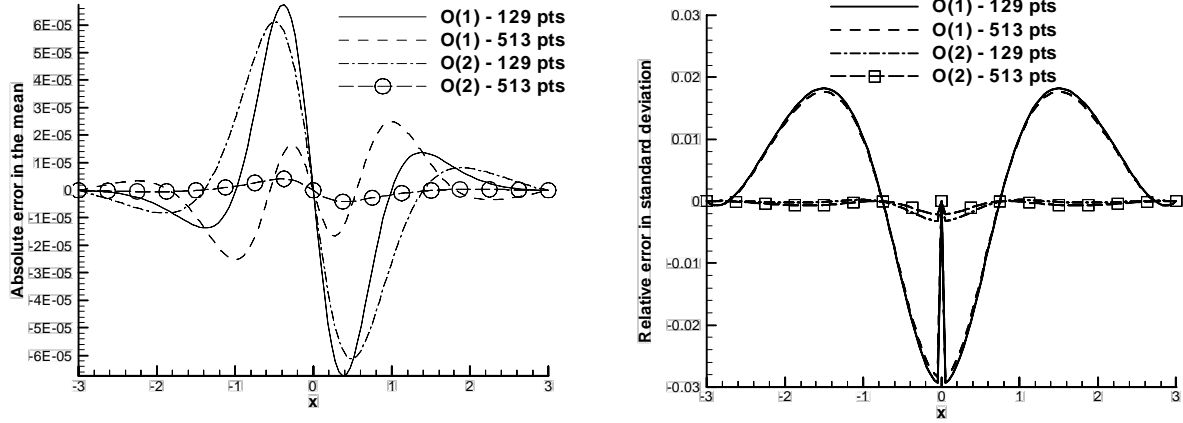


FIG. 4.11. Absolute error in the mean (left) and relative error in the standard deviation (right) from Polynomial Chaos.

Provided that the PDF of the output uncertainty on the boundary is known, one can determine the required modal values,  $u_i$ , on the boundary by matching moments as was done here. It is not likely that the PDF will be available for general CFD simulations. Moreover, we will be fortunate to get good estimates of the mean and variance at the boundaries. In the absence of higher order statistics, one is forced to make assumptions that degrade the error reduction rate of the method. However, as shown earlier, even relatively low-order ( $<3$ ) chaos can produce results superior to the first- and second-moment methods.

To further demonstrate the boundary condition issue, the right of Figure 4.12 shows the error convergence for a slightly simpler problem, the  $1-D$  heat equation with internal heat generation. The significant difference between these two problems is the stochastic boundary conditions. For the heat equation, the domain is finite and the boundary conditions, by problem definition, have no uncertainty. The uncertainty enters through the thermal conductivity which was treated as a Gaussian random variable with a  $CoV = 10\%$ . This problem has a simple exact stochastic solution and since there is no boundary uncertainty, the exact boundary condition treatment is to set all higher modes to zero. As seen, the exponential convergence rate is achieved. On the other hand, for the Burgers equation, the effect of not being able or willing to specify the higher modes exactly results in the “peeling off” of the error from the theoretical curve.

Further impact of the boundary condition specification for the Burgers equation can be seen in Figure 4.13 in which the exact solution is compared with the probability density function of a third-order chaos at  $x = -2$ ; the shaded areas highlight their difference. The three boundary conditions correspond to specification of the mean (BC1), mean and variance (BC2), mean, variance, and skewness (BC3) respectively, i.e., the boundary condition specifications are increasingly complete. The first boundary condition shows that ignoring the variance at the boundary results in a much more peaked distribution than should be predicted. This effect is even more pronounced closer to the boundary on which there is no distribution, just a mean value and zero variance. Consequently, moving slightly inward results in some but little variance since it’s forced to zero nearby, and hence a large narrow peak. However, as seen in the lower left of the figure, addition of the variance makes substantial improvement in the prediction although the distribution is Gaussian. Providing additional information concerning the boundary skewness is seen to shift the distribution markedly such that the interior skewness is now well predicted.

TABLE 4.2  
Case description for Figure 4.12

Case	Boundary Condition	Grid Points
1	Mean only	129
2	Mean and Variance	129
3	Mean, Variance, and Skewness	129
4	Mean, Variance, and Skewness	257
5	Mean, Variance, and Skewness	513

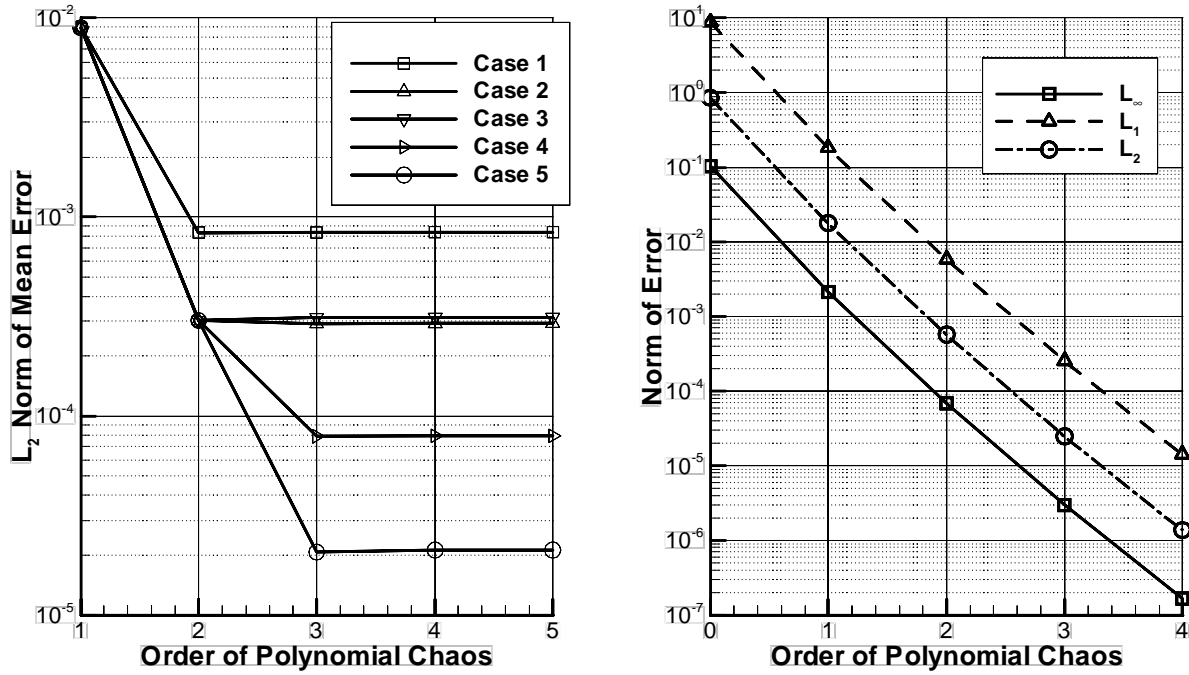


FIG. 4.12. Error in the mean for various orders of Polynomial Chaos. Left - Burger's equation with various boundary conditions and grids. Right - Heat equation with stochastic internal heat generation..

The statistics of the distribution predicted by a 4<sup>th</sup> order chaos are compared with the exact solution in Figure 4.14. Without symbols on the plots, the distributions are all but indistinguishable. Note that the standard deviation is a maximum in the vicinity of  $x = \pm 1$  where the PDF is nearly Gaussian as indicated by its skewness near 0 and kurtosis value near 3. The PDF's switch from skewed to the left to skewed to the right in each half domain  $x \in [-3, 0]$  and  $x \in \{0, 3]$ . It is also clear that the departure from Gaussian is maximal at the boundary.

An estimate of the computational effort associated with this problem is shown in Figure 4.15. The deterministic, first- and second-order moment methods, and polynomial chaos of orders 1-3 are compared with the cost of 100 Monte Carlo simulations. Moment methods cost 2-3 times more than a deterministic solution. The work of polynomial chaos is relatively high, about 20 times the cost of a deterministic solution but there are opportunities to reduce this cost (e.g. loosely-coupled algorithms, multi-grid, ...).

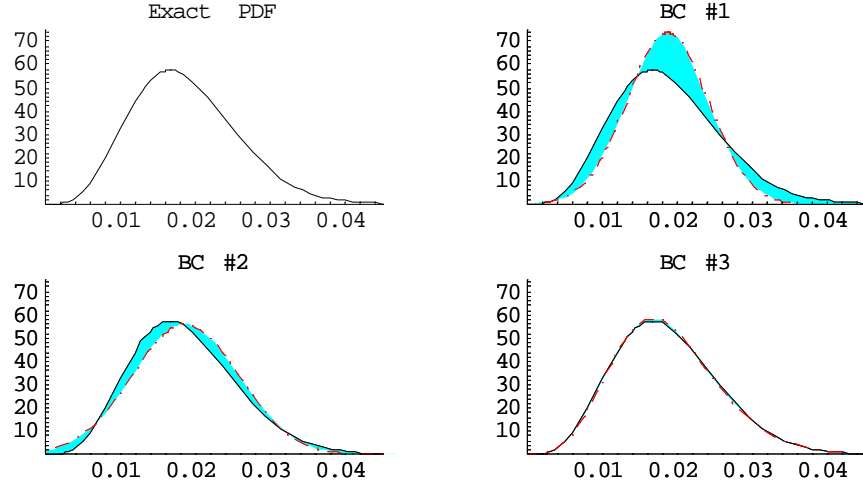


FIG. 4.13. Comparison of exact and polynomial chaos pdf's at  $x = -2$  with three different boundary conditions. The shaded areas highlight the difference between the exact and approximate PDF's.

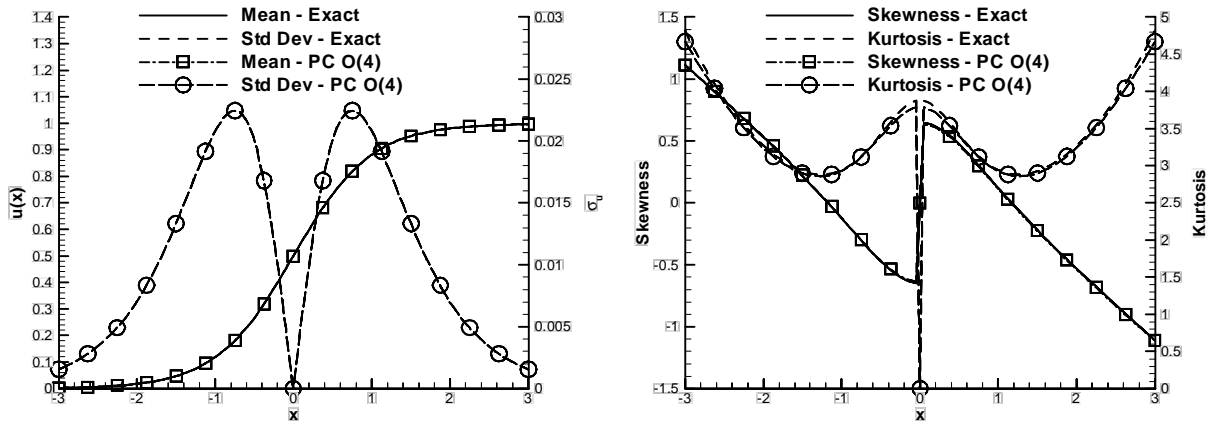


FIG. 4.14. Statistics of the output distribution from 4<sup>th</sup> order Polynomial Chaos compared with the exact solution.

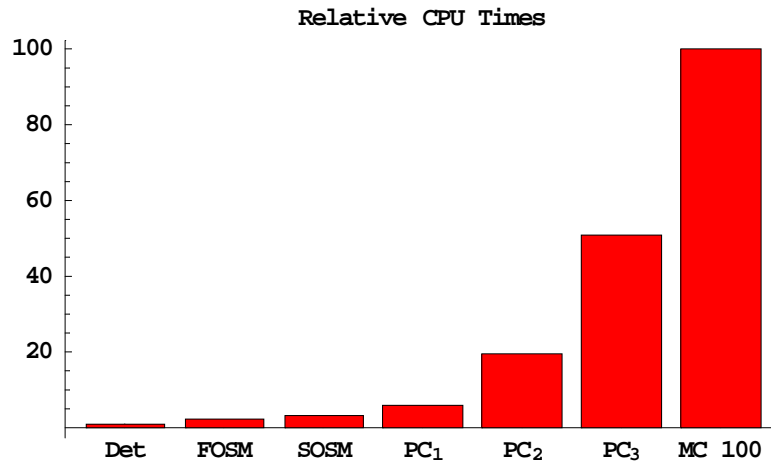


FIG. 4.15. Relative cpu times to generate solutions to the Burger equation.



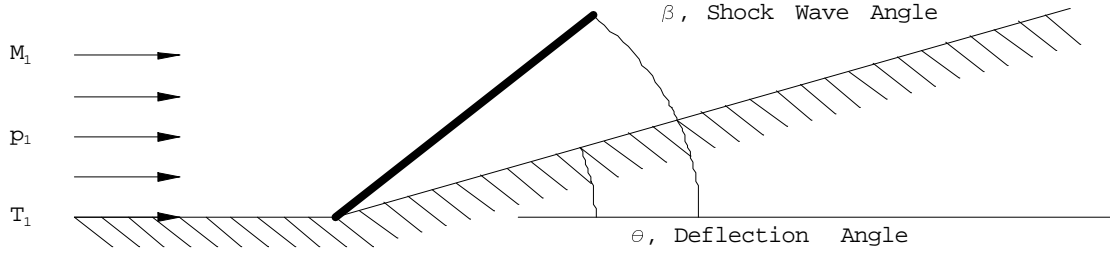


FIG. 5.1. Sketch of supersonic, inviscid flow over a wedge.

**5. Oblique Shock Waves.** Shock waves and expansion fans are fundamental building blocks for inviscid compressible flow theory. We begin by addressing inviscid, supersonic flow over a wedge at Mach numbers and wedge angles for which an attached, steady, oblique shock forms. A sketch of the problem is shown in Figure 5.1. The output quantity of interest for this example is the pressure rise across the shock wave,  $\frac{p_2}{p_1}$ , which is strictly a function of the upstream Mach number,  $M_1$  and the wedge angle  $\theta$  (for a fixed  $\gamma$ ). In all cases, we take the ratio of specific heats,  $\gamma = 1.4$ .

**5.1. Deterministic Problem.** For a perfect gas, the pressure rise across a normal shock wave is given by the Rankine-Hugoniot relation

$$(5.1) \quad \frac{p_2}{p_1} = 1 + \frac{2\gamma}{\gamma + 1}(M_1^2 - 1)$$

where the subscripts “1” and “2” refer to conditions just ahead of and behind the shock wave respectively.

The pressure rise across an oblique shock can be obtained from the normal shock relation by replacing the Mach number in Eq.(5.1) by the normal component of the upstream Mach number,  $M_{1n}$  in this case. From geometric considerations,

$$(5.2) \quad M_{1n} = M_1 \sin \beta.$$

A relationship for the shock wave angle,  $\beta$ , can be obtained from the tangential momentum equation (the so-called  $\beta - \theta - M$  relationship). A common form of this relationship is

$$(5.3) \quad \tan \theta = 2 \cot \beta \left\{ \frac{M^2 \sin^2 \beta - 1}{M^2(\gamma + \cos 2\beta) + 2} \right\}.$$

For a detailed derivation, see e.g. [5]. Note that this relationship uniquely specifies the flow deflection angle,  $\theta$ , for a given Mach number ahead of the shock, (denoted generically by  $M$ ) and shock wave angle,  $\beta$ . However, in practice, one generally knows the Mach number and the geometry,  $\theta$ , (to within a manufacturing tolerance), thus, one needs to solve Eq.(5.3) for  $\beta$ . With some manipulation, this equation can be written as a cubic polynomial in the variable  $\sin^2 \beta$ , hence three solutions for  $\beta$  exist for each  $\{M, \theta\}$  pair. Two of the solutions correspond to physical processes that occur in nature: a strong shock wave and a weak shock wave although the latter is preferred by nature and is the one we study here. The third solution is non-physical. Frequently, one uses a numerical root finding procedure such as the Secant method to iteratively solve Eq.(5.3) for the value of  $\beta$  corresponding to the weak solution but here we used the analytic solution (obtained via Mathematica v4 [46]). This was especially useful for computing exact analytic sensitivity derivatives for this problem. A plot of the  $\beta - \theta - M$  relationship is shown on the left of Figure 5.2 for selected Mach numbers. As can be seen, for each Mach number there is a maximum deflection angle beyond

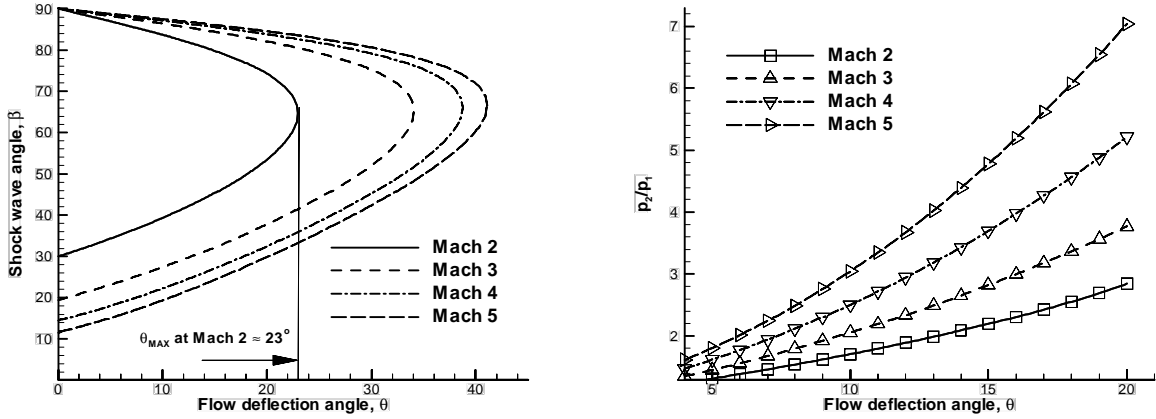


FIG. 5.2. (left)  $\beta - \theta - M$  relationship for various Mach numbers. (right) pressure rise from the deterministic solution.

which no solutions exist. At Mach 2, the maximum deflection is approximately  $23^\circ$ , at Mach 5 it is roughly  $41^\circ$ .

Once  $\beta$  is found, one solves Eq.(5.2) for the normal component of the Mach number and replaces  $M_1$  by  $M_{1_n}$  in Eq.(5.1) to obtain the deterministic values of the pressure rise. Other than the assumptions already mentioned (i.e., inviscid, perfect gas) which arise in the governing equations, this procedure is exact. The solution for the pressure rise across an oblique shock is shown on the right of Figure 5.2.

A far more general albeit expensive approach to solving this problem is to use modern CFD techniques. To that end, we used the two-dimensional CFD code, FLOW.f (formerly ANSERS) supplied by A. Taylor. This code solves the Navier-Stokes equations and subsets including the Euler equations on finite volume meshes using upwind discretization methods (see [44]). A sample result of one calculation is shown in Figure 5.3 for which pressure contours over the wedge corresponding to the conditions  $M_\infty = 3$  and  $\theta = 5^\circ$  are displayed. To compare the CFD calculations with oblique shock relations, we took the pressure behind the shock to be the cell-averaged value from the last cell on the surface (i.e., right before the exit plane). On  $31 \times 46$  grids, the results of the CFD calculations at all Mach numbers considered are visually indistinguishable on the pressure rise plot from the exact oblique shock results.

**5.2. Stochastic Problem.** Two variables, the Mach number,  $M$ , and wedge angle,  $\theta$ , were considered to be Gaussian random variables, both with a coefficient of variation of 10%. The main focus was on the geometric uncertainty associated with the wedge angle. The uncertainty analysis methods implemented were Monte Carlo and the first-order moment method for which the first-order sensitivity derivatives were computed analytically. For example, to compute the sensitivity derivative  $\frac{\partial p}{\partial \theta}$  we used the chain rule,

$$(5.4) \quad \frac{\partial p}{\partial \theta} = \frac{\partial p}{\partial M_{1_n}} \frac{\partial M_{1_n}}{\partial \beta} \frac{\partial \beta}{\partial \theta}.$$

The first two terms are trivial but the third is essentially impossible by hand. Mathematica version 4 [46] was used to evaluate  $\frac{\partial \beta}{\partial \theta}$  analytically, although other approaches, including numerical derivatives could be used. The results of the sensitivity derivative evaluation are shown in Figure 5.4. Note that the derivative is fairly linear until  $\theta$  approaches the maximum flow deflection angle at which point the derivative varies very rapidly. This is just another example of the highly non-linear nature of fluid mechanics.

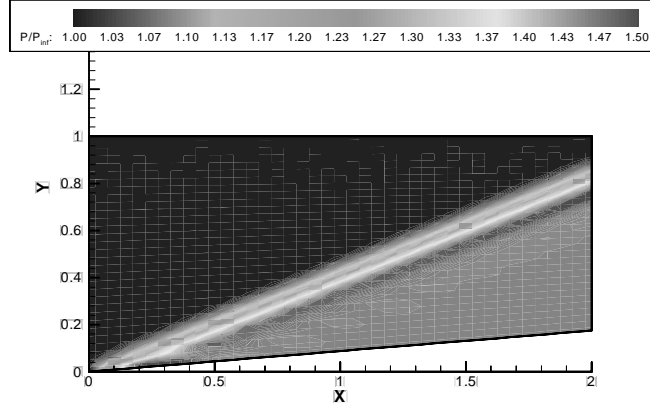


FIG. 5.3. Non-dimensional pressure contours for Mach 3 flow over a  $5^\circ$  wedge. Second-order accurate upwind solution from FLOW.f on a  $31 \times 46$  mesh.

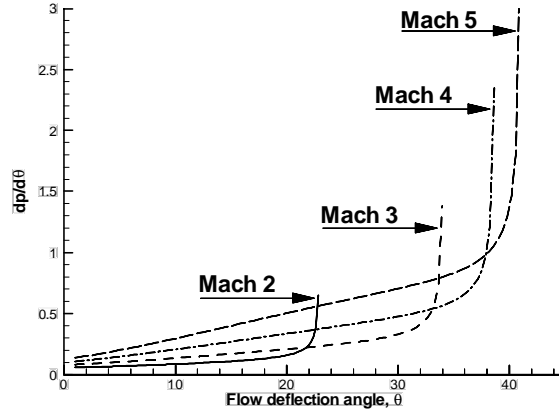


FIG. 5.4. Non-dimensional sensitivity derivative of pressure with respect to deflection angle. Note the highly non-linear nature in the vicinity of the maximum deflection angle for each Mach number..

Monte Carlo simulations using both oblique shock relations and CFD were run for mean Mach numbers  $\{M = 2, 3, 4, 5\}$  and mean flow deflection angles  $\{\theta = 5^\circ, 10^\circ, 15^\circ, 20^\circ\}$ . For each case, 1000 simulations were performed. Additionally, correlations between the two random variables were investigated. For each  $\{M, \theta\}$  pair, the correlation coefficient,  $\rho$ , was varied from  $\{-1, 1\}$  resulting in  $9 \times 16 \times 1000 = 144,000$  2D CFD simulations and an equal number of oblique shock calculations. The CFD calculations were performed at ICASE on 8-processors of CORAL. It took approximately two overnight runs to complete the 144,000 simulations. The oblique shock relations were run in a matter of minutes on a 200 MHz pentium PC. In terms of the statistics of the distributions, both approaches yielded consistently similar values. The expected value of the pressure rise with 95% mean confidence intervals and the coefficient of variation are shown in Figure 5.5.

Note that the data point corresponding to  $M = 2$ ,  $\theta = 20^\circ$  is missing. For a Gaussian distributed random variable with a mean of  $20^\circ$  and standard deviation of  $2^\circ$  (i.e., 10% CoV), the 95% confidence region

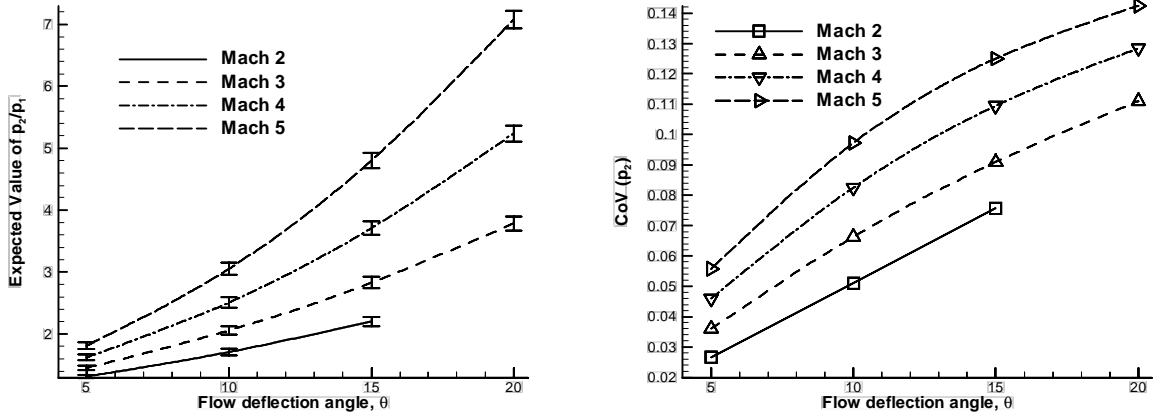


FIG. 5.5. (left) Mean pressure rise for an input  $CoV[\theta]=0.1$ . The error bars represent 95% mean confidence intervals from 1000 Monte Carlo simulations. (right) output pressure coefficient of variation. The “bad” point at Mach 2,  $\theta = 20^\circ$  is due to sampling values of  $\theta$  greater than  $\theta_{Max}$ .

TABLE 5.1  
Number of samples from  $N[20,2]$  that are greater than  $\theta$  (out of 1000).

$\theta^\circ$	Number of Samples $> \theta$	
	Exact Values	Random Draw
20	500	492
21	309	292
22	159	143
23	67	73
24	23	24
25	6	8
26	1	2

is roughly  $[16^\circ, 24^\circ]$ . Clearly, when randomly drawing 1000 samples from such a distribution, numerous samples will be drawn with values greater than  $23^\circ$  (see Table 5.1) which corresponds to the maximum flow deflection angle for this Mach number hence the  $M = 2, \theta = 20^\circ$  data point was rejected. To further illustrate this, Figure 5.6 shows the input histogram with mean angle of  $20^\circ$  where numerous samples greater than  $23^\circ$  can be seen. The center and right histograms are the pressure output for input conditions  $M = 2, \theta = 15^\circ$  and  $M = 5, \theta = 20^\circ$ , respectively for which all of the sampled angles are well below  $\theta_{Max}$  for each Mach number. In this rather academic example, we chose large variations in the input variables purposely to make the graphics easier to see, but for one case, this resulted in non-physical sampling. Such is likely to occur with many random variables that may arise in fluid mechanics applications, for example, thermodynamic and transport properties are bounded from below by zero whereas a Gaussian distribution has support on  $[-\infty, \infty]$ . One approach to overcoming this problem is to either truncate the distribution or to use distributions with finite support (such as the Beta distribution) provided that the use of such a distribution can be justified.

For demonstration purposes, correlations between the upstream Mach number and  $\theta$  were considered.

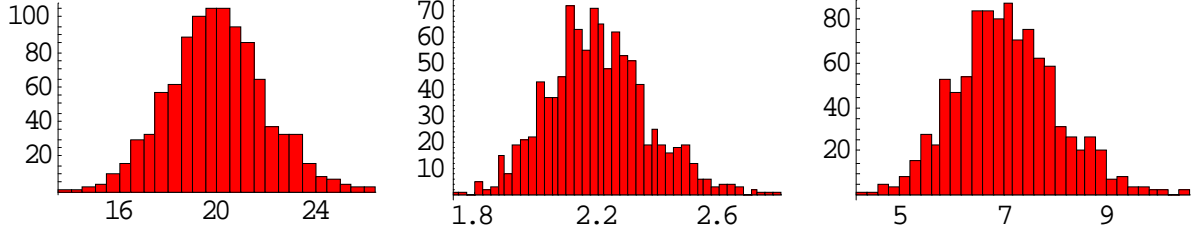


FIG. 5.6. Histograms of: (left) input wedge angles from  $N[20,2]$ , (center) output pressure at  $M = 2$ ,  $\theta = 15^\circ$  and (right) output pressure at  $M = 5$ ,  $\theta = 20^\circ$ .

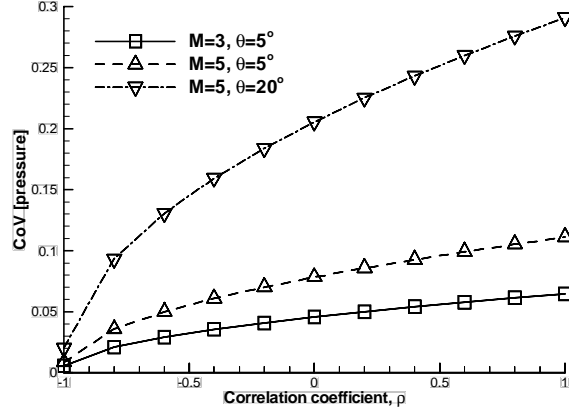


FIG. 5.7. Output pressure coefficient of variation due correlation of free-stream Mach number and wedge angle,  $\theta$ .

The result of correlating these variables is shown in Figure 5.7. As expected, when  $M$  and  $\theta$  are positively correlated, the combined model uncertainty increases since increasing  $M$  or  $\theta$  independently increases the uncertainty. Likewise, negative correlation reduces the variance since one tends to offset the other. Note that a rather substantial variation with correlation coefficient occurs particularly for the stronger cases (larger mean  $M$  and mean  $\theta$ ). Clearly, when considering multiple random input variables, it will be important to have knowledge of the correlation among the variables in order to get reliable output estimates of the variance.

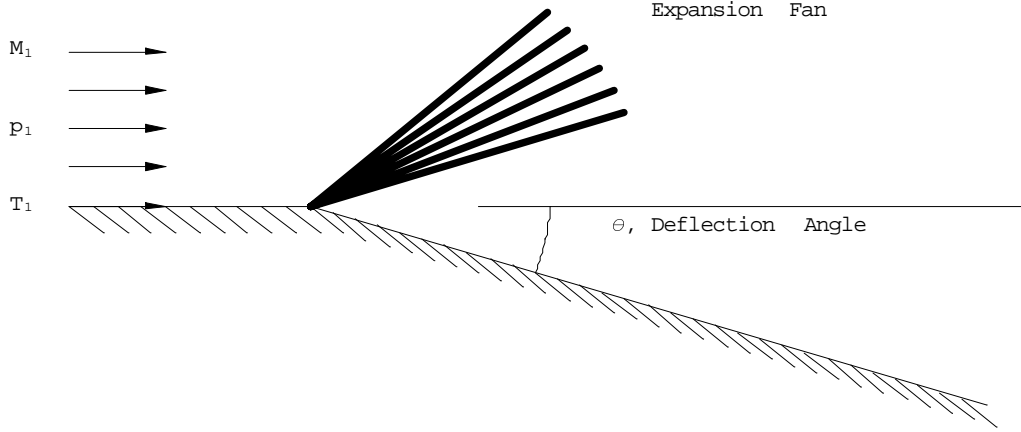


FIG. 6.1. Sketch of supersonic flow over an expansion corner.

**6. Prandtl-Meyer Expansion Waves.** Expansion waves form another fundamental building block for compressible flow theory. In this case, we consider the flow of a calorically perfect gas across a centered expansion fan emanating from a sharp convex corner as shown in the sketch of Figure 6.1. We take the output quantity of interest to be the pressure drop through the expansion fan which is a function of the upstream Mach number and flow turning angle.

**6.1. Deterministic Problem.** The solution to this supersonic flow problem was first presented by Prandtl in 1907 and subsequently by Meyer in 1908 [5]. The basic problem is to determine properties behind the rearward Mach line given flow properties ahead of the expansion corner. The governing differential equation for this flow is

$$(6.1) \quad d\theta = \sqrt{M^2 - 1} \frac{dV}{V}$$

where  $V$  is the flow velocity and  $d\theta$  is an infinitesimally small expansion angle. Integrating the differential equation over the entire expansion angle yields,

$$(6.2) \quad |\Delta\theta| = \nu(M_2) - \nu(M_1)$$

where the notation  $\Delta\theta$  implies the total turning angle that the flow experiences and  $\nu(M)$  is the Prandtl-Meyer function, which for a calorically perfect gas, is

$$(6.3) \quad \nu(M) = \sqrt{\frac{\gamma+1}{\gamma-1}} \tan^{-1} \sqrt{\frac{\gamma-1}{\gamma+1} (M^2 - 1)} - \tan^{-1} \sqrt{M^2 - 1}.$$

Given the upstream Mach number,  $M_1$ , and the flow expansion angle,  $|\Delta\theta|$ , the procedure for solving this problem is:

1. compute  $\nu(M_1)$  from Eq.(6.3)
2. compute  $\nu(M_2)$  from Eq.(6.2)
3. compute  $M_2$  by solving Eq.(6.3) as a root-finding problem or find  $M_2$  from tabulated values
4. Use isentropic relations to compute flow properties in region 2

For example, the pressure decrease,  $p_2/p_1$ , can be obtained from

$$(6.4) \quad \frac{p_2}{p_1} = \left[ \frac{1 + \frac{\gamma-1}{2} M_2^2}{1 + \frac{\gamma-1}{2} M_1^2} \right]^{\frac{\gamma}{1-\gamma}}.$$

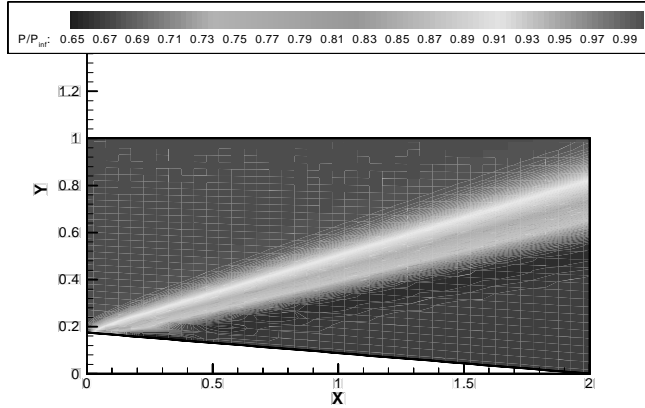


FIG. 6.2. Non-dimensional pressure contours for Mach 3 flow over a  $5^\circ$  expansion corner. Second-order accurate upwind solution from FLOW.f on a  $31 \times 46$  mesh.

The second approach that we used to solve this problem was the flow analysis code FLOW.f described earlier. Simple h-meshes consisting of  $31 \times 46$  grid points were used for the simulations. Pressure contours from a Mach 3 simulation over a  $5^\circ$  expansion corner are shown in Figure 6.2. For comparisons with the Prandtl-Meyer results, we again took the discrete value of the pressure behind the expansion to be the cell-averaged value at the last cell on the surface ahead of the exit plane.

**6.2. Stochastic Problem.** Similar to the oblique shock wave example, we took the upstream Mach number and the flow expansion angle to be Gaussian random variables with a coefficient of variation of 10%. Monte Carlo simulations (1000 per case) and the first-order moment method were implemented using both analysis methods discussed. The expected value of the pressure decrease shown in Figure 6.3 closely follows the deterministic solution. On the original  $21 \times 31$  grids used by the CFD code, we found discrepancies at the higher Mach numbers and turning angles. Consequently, we refined the grids to  $31 \times 46$  for which solutions at all  $\{M, \theta\}$  pairs compared closely to the exact solution.

Sensitivity derivatives were computed using finite-differencing of the exact inviscid Prandtl-Meyer solution. Results for the pressure sensitivity are shown in the right of Figure 6.3. For moderate turns of less than approximately  $10^\circ$ , pressure sensitivity increases with increasing Mach number, but at higher turning angles, this trend reverses. Since the first-order estimate of the standard deviation is directly proportional to the pressure sensitivity  $\frac{\partial p}{\partial \theta}$ , this behavior is reflected in the standard deviation of the pressure distribution (see Figure 6.4). However, the relative uncertainty in terms of the coefficient of variation monotonically increases with increasing Mach numbers and turning angles. Note that quite substantial variation in the output occurs at the higher  $\{M, \theta\}$  pairs.

We implemented the bootstrap estimate of the standard error to compute confidence intervals for any statistical quantity. The method has the advantage that it is easy and efficient to implement, general in the sense that it is not restricted to a specific distribution, e.g. a Gaussian, and it can be completely automated for any estimator. The interested reader is referred to [12] for details of the method. In practice, one takes 25 – 200 bootstrap samples to obtain a standard error estimate. Table 6.1 shows bootstrap standard error estimates of the mean, standard deviation, and coefficient of variation for a range of bootstrap sample numbers for the case of Mach 5 flow over an expansion corner with a mean angle of  $20^\circ$  and a coefficient

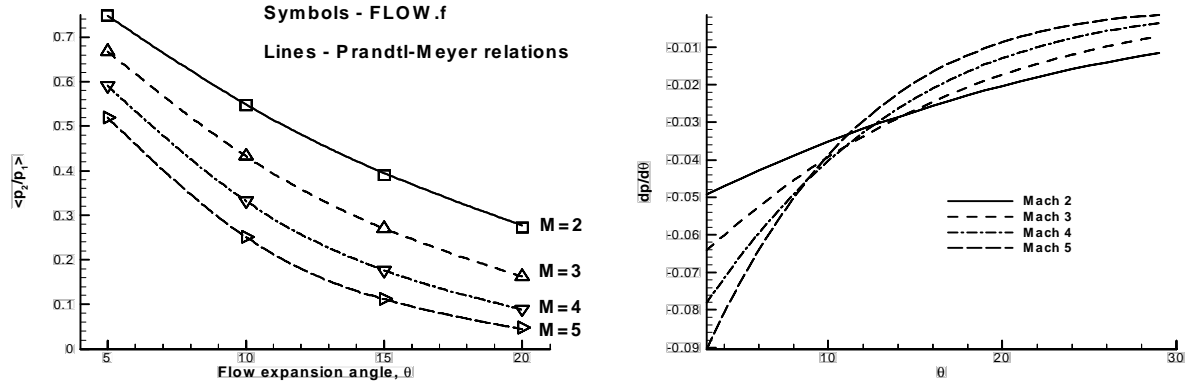


FIG. 6.3. (left) Expected value of the pressure decrease through an expansion from 1000 Monte Carlo simulations. (right) Sensitivity derivatives.

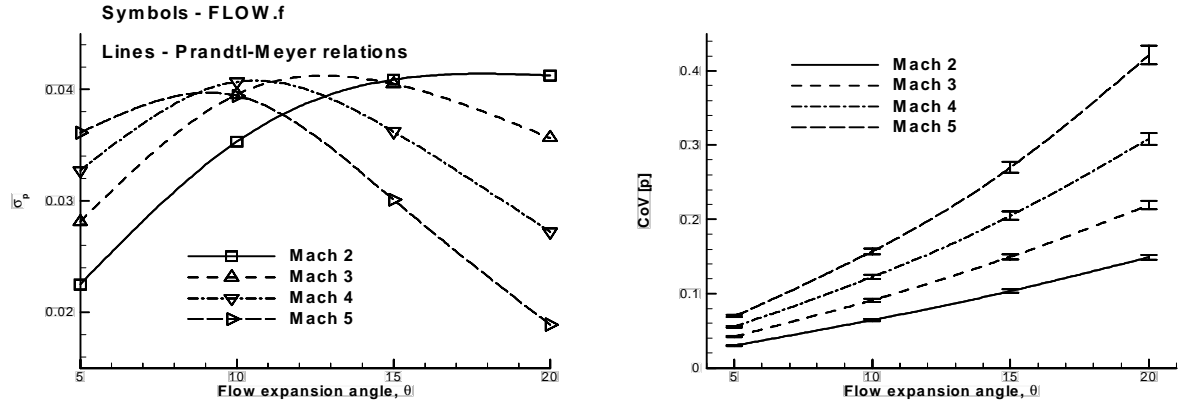


FIG. 6.4. Pressure output: (left) Standard deviation and (right) coefficient of variation with 95% mean confidence intervals from 1000 Monte Carlo simulations.

of variation of 10%. The 95% confidence intervals shown in Figure 6.5 were obtained from the bootstrap estimate of the standard error in the coefficient of variation of pressure.

The histogram in Figure 6.6 shows that the random variable  $p_2/p_1$  is non-Gaussian as evidenced by the significant tail to the right. Results of the analysis assuming correlation among the  $\{M, \theta\}$  pairs are presented in Figure 6.6. The trends are similar to the oblique shock results in that positively correlated variables result in the greatest uncertainty. This is intuitive since increasing the expansion angle results in greater uncertainty as does independently increasing the Mach number.

**7. Supersonic Airfoil.** Shock-expansion theory has been used extensively to model supersonic flow over thin airfoils. This example considers steady, two-dimensional adiabatic flow of an inviscid, perfect gas over the airfoil shape described by its upper and lower surfaces,  $y_u(x)$  and  $y_l(x)$ , respectively. The airfoil coordinates are given by

$$(7.1) \quad y_u(x) = \frac{t}{2} \cos\left[\pi\left(\frac{x}{c} - \frac{1}{2}\right)\right], \quad y_l(x) = -y_u(x), \quad x \in [0, c].$$



TABLE 6.1

Estimates of standard error for various bootstraps samples from Mach 5 flow over an expansion corner with a mean angle of 20 degrees and a coefficient of variation of 10 percent.

Number of Bootstraps	Standard Error in the Mean	Standard Error in $\sigma$	Standard Error in CoV
100	0.000547105	0.000751298	0.0144571
200	0.000598759	0.000673770	0.0138239
300	0.000557259	0.000678446	0.0137223
400	0.000581007	0.000674247	0.0133587
500	0.000600424	0.000691841	0.0134268

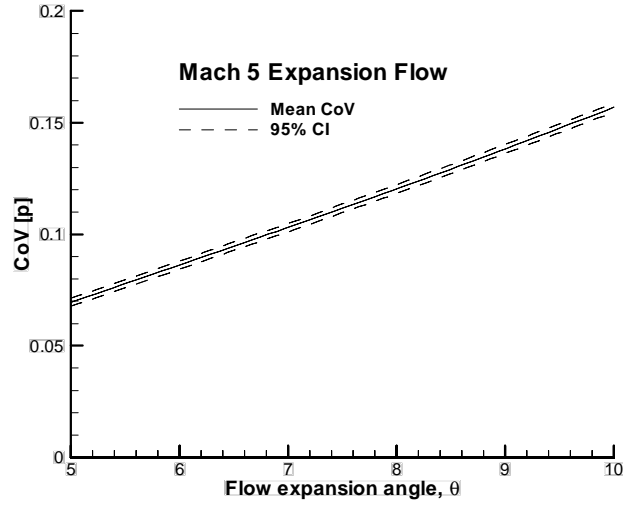


FIG. 6.5. Application of the bootstrap error estimator for confidence intervals.

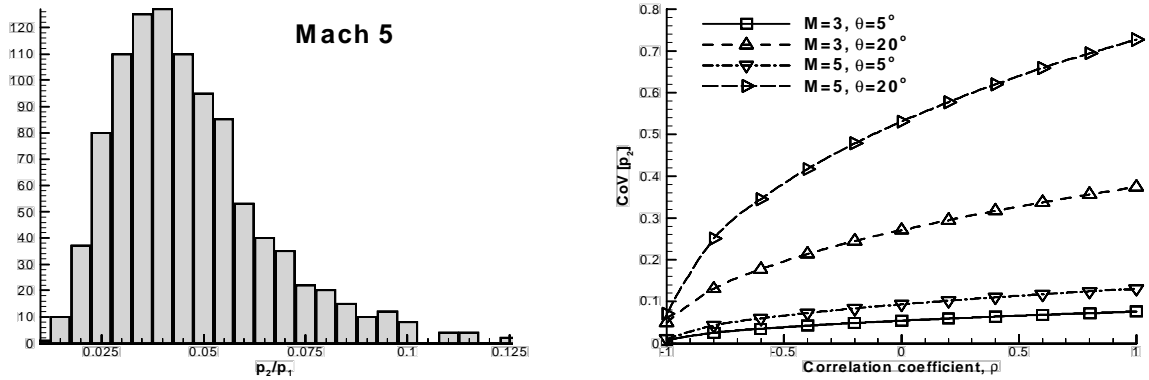


FIG. 6.6. Left - Output pressure coefficient of variation due correlation of free-stream Mach number and wedge angle,  $\theta$ . Right - Histogram of the output pressure distribution at Mach 5 through an expansion with a mean angle of 20° and a 10% coefficient of variation. Note that the distribution is skewed to the right.

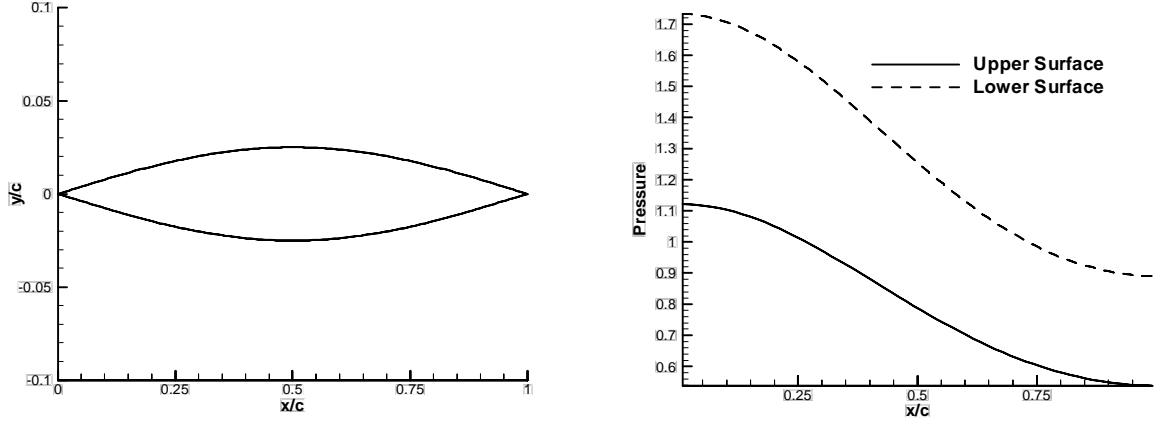


FIG. 7.1. Surface coordinates (left) and pressure distribution corresponding to  $M_\infty = 3$  and  $\alpha = 3^\circ$  (right).

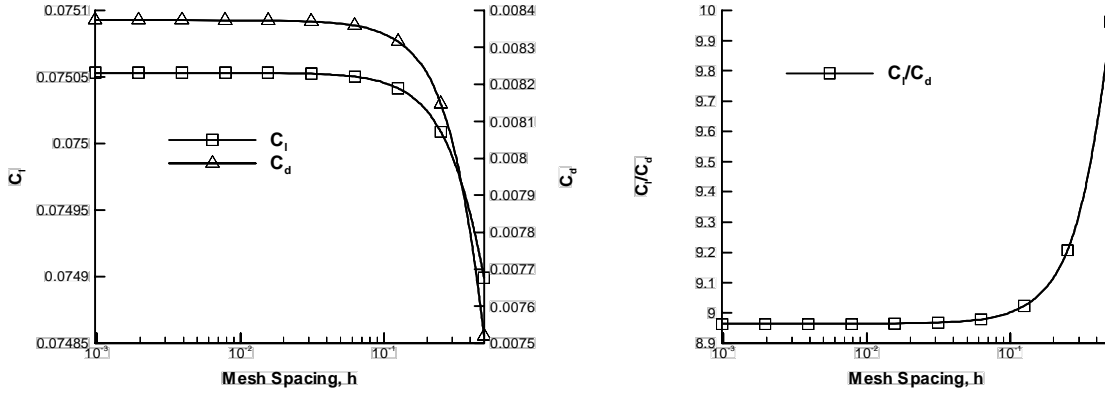


FIG. 7.2. Grid convergence results for the thin supersonic airfoil at Mach 3 and an angle of attach of 3 degrees.

The shape of the airfoil is shown in Figure 7.1. Visually, the airfoil is displayed five times thicker than it actually is due to the aspect ratio of the plot. For all calculations, the free-stream Mach number was fixed at three, ( $M_\infty = 3$ ). The non-dimensional pressure distribution obtained on a uniform 65 grid point ( $h = 0.016$ ) mesh at an angle of attack,  $\alpha = 3^\circ$  and a thickness-to-chord ratio,  $\frac{t}{c} = 0.05$ , is shown on the right.

Grid convergence studies were performed prior to generating stochastic solutions. Ten grid levels were used with the number of points,  $n$ , determined from  $n = 2^i + 1$ ,  $i = \{1, 2, \dots, 10\}$ . The mesh size,  $h \equiv \frac{\Delta x}{c} = \frac{1}{n-1}$  varies from a maximum value of 0.5 to the minimum of 0.000976563. Figure 7.2 shows the results of this grid refinement process on  $C_l$ ,  $C_d$ , and  $C_l/C_d$ . As can be seen, grid convergence occurs fairly quickly. On the 65 grid point ( $h \approx 0.016$ ) mesh corresponding to the sixth level of refinement (starting from a *very* coarse 3 grid point, 2 panel airfoil), the solution is converged for all practical purposes.

For the stochastic calculations, the thickness-to-chord ratio was assumed to behave as a Gaussian random variable with a mean value of  $\frac{t}{c} = 0.05$  and a coefficient of variation of 1%. Solutions on a 65 grid point mesh were generated by the Monte Carlo method and the first- and second-moment methods. The sensitivity

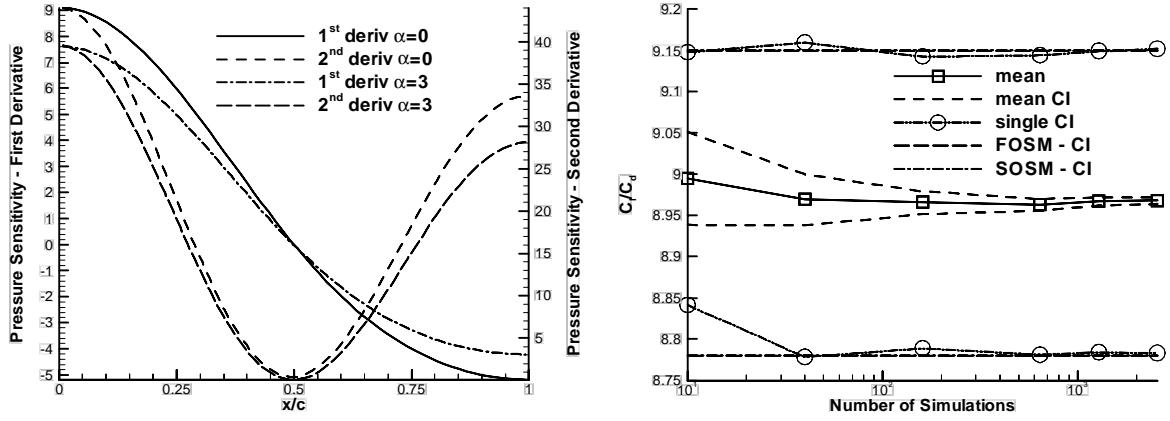


FIG. 7.3. Monte Carlo convergence history. The FOSM and SOSM results are shown for reference.

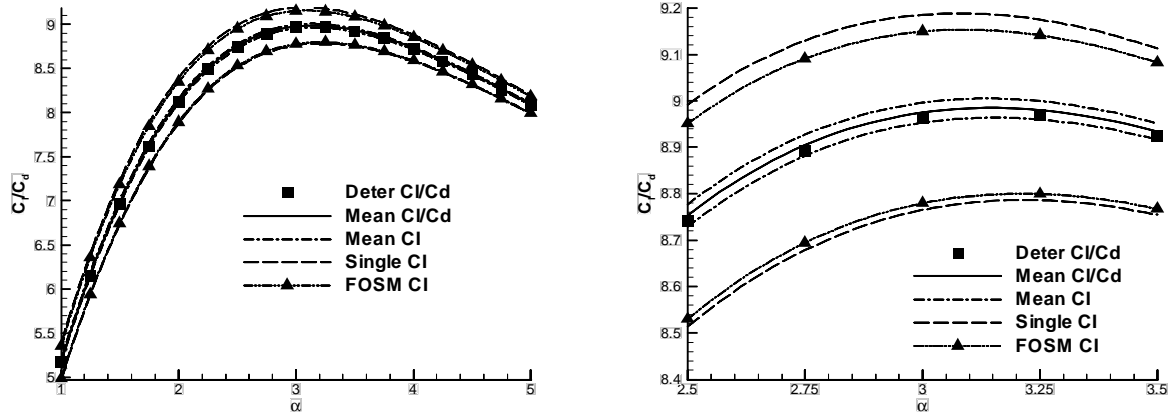


FIG. 7.4. Expected value of lift-to-drag coefficients with uncertainty due to a 1% coefficient of variation in airfoil thickness.

derivatives with respect to  $\frac{t}{c}$  required by the moment methods were computed using second-order accurate finite differences. The upper surface pressure sensitivity derivatives versus  $x/c$  for two different angles of attack ( $\alpha = 0^\circ$  and  $3^\circ$ ) are shown in Figure 7.3. Three function evaluations per angle-of-attack are required by this procedure. If one is only interested in a single output quantity, such as  $C_l/C_d$ , there is no need to compute the pressure sensitivities since the sensitivity derivative of the output quantity can be determined directly from the differencing procedure. Figure 7.3 shows the Monte Carlo convergence of the expected value of  $C_l/C_d$  and 95% mean and single prediction confidence intervals.

Finally, the performance of the airfoil across a range of angles of attack was studied. The angle-of-attack was varied from  $1^\circ$  to  $5^\circ$  in increments of  $1/4^\circ$ . Results from 100 Monte Carlo simulations for each angle-of-attack are compared with results from the first-order moment method in Figure 7.4 where again good correspondence between the FOSM confidence interval and the single prediction confidence interval is seen. The enlarged view on the right clearly shows that FOSM slightly underestimates the variance. The second-order moment method produces results virtually identical to FOSM and were omitted for clarity.

**8. Laminar Boundary Layer Flow.** The boundary layer equations for steady, two-dimensional incompressible flow with constant properties can be written as

$$(8.1) \quad \frac{\partial u}{\partial x} + \frac{\partial v}{\partial y} = 0$$

$$(8.2) \quad u \frac{\partial u}{\partial x} + v \frac{\partial u}{\partial y} = U \frac{dU}{dx} + \nu \frac{\partial^2 u}{\partial y^2}$$

subject to the boundary conditions

$$(8.3) \quad u(x, 0) = v(x, 0) = 0 \quad u(x, \infty) = U(x).$$

It is well known that these partial differential equations can be re-cast in terms of a similarity variable as an ordinary differential equation for which solutions exist for specific freestream velocity distributions,  $U(x)$ . In 1908, Blasius found a solution to the parallel flow over a flat plate with  $U(x)$  a constant (see [45]). Under these conditions, the governing equations in self-similar form reduce to

$$(8.4) \quad f''' + f f'' = 0$$

where  $f = f(\eta)$  only and

$$(8.5) \quad u(x, y) = U(x) f'(\eta) \quad \text{where} \quad \eta(x, y) = y \sqrt{\frac{U}{2\nu x}}.$$

The boundary conditions transform to

$$(8.6) \quad f(0) = f'(0) = 0 \quad f'(\infty) = 1$$

To date, an analytic solution to this equation is not known although series solutions with a finite radius of convergence are established. Numerically, the problem reduces to finding the value of  $f''(0)$  such that  $f' \rightarrow 1$  as  $\eta \rightarrow \infty$ . An asymptotic analysis shows that  $\eta = 10$  is a sufficiently large value. Finding the correct value of  $f''(0)$  is a simple root finding problem which, in our calculations, was solved by the Secant method. The correct value to six significant digits is (see [45])

$$(8.7) \quad f''(0) = 0.469600 \dots$$

**8.1. Deterministic Problem.** A relatively fine 5000 grid point mesh distributed on  $\eta \in [0, 10]$  was used for the numerical solution. Similarity functions and velocity profiles  $x = 1$  meter for three different freestream Reynolds numbers ( $Re \equiv \frac{Ux}{\nu}$ ) are shown in Figure 8.1.

**8.2. Stochastic Problem.** The kinematic viscosity,  $\nu$ , was taken as a normally distributed stochastic input parameter with a coefficient of variation of 2%. The sensitivity derivative required for the FOSM method can be obtained from

$$(8.8) \quad \frac{\partial u}{\partial \nu} = \frac{\partial u}{\partial \eta} \frac{\partial \eta}{\partial \nu} = -\frac{U\eta}{2\nu} f''(\eta).$$

The second derivative (for the SOSM method) can be found by further application of the chain rule to be

$$(8.9) \quad \frac{\partial^2 u}{\partial \nu^2} = \frac{U\eta}{4\nu^2} (3f''(\eta) + \eta f'''(\eta)).$$

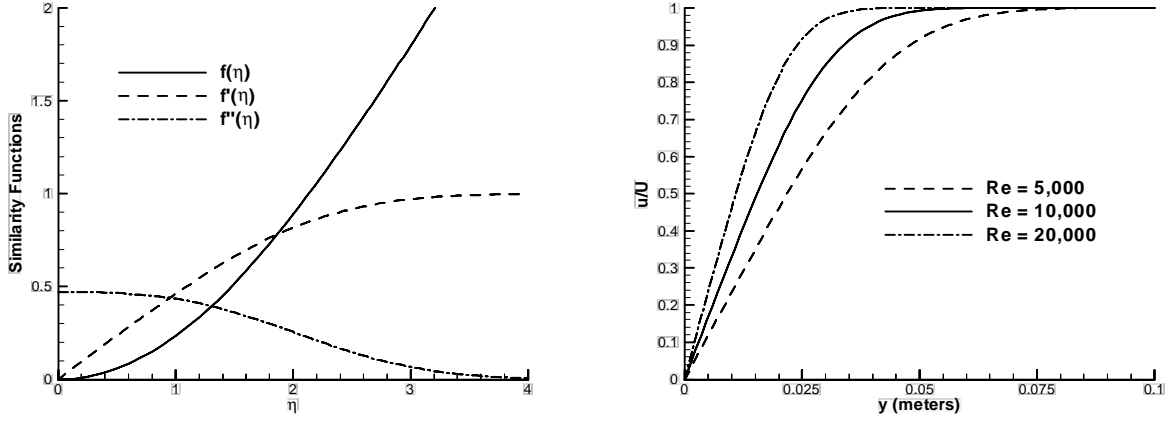


FIG. 8.1. Blasius solution for the flow over a flat plate. Function profiles (left) and velocity distributions at three Reynolds numbers (right).

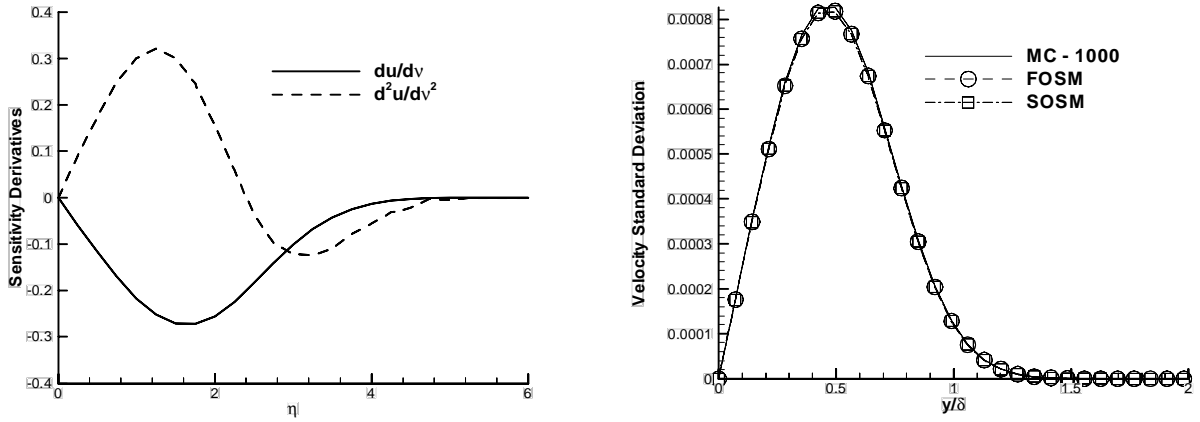


FIG. 8.2. Non-dimensional sensitivity derivatives (left) and distribution of the velocity standard deviation through the boundary layer.

Plots of the derivatives, non-dimensionalized by  $U$  and the mean viscosity,  $\bar{\nu}$ , are shown in Figure 8.2. For this problem, the contribution of the second derivative terms to the estimates of the mean and variance are negligibly small and hence their distributions are indistinguishable as seen on the right of Figure 8.2 where the Monte Carlo results after 1000 simulations are also shown for comparison.

Mean velocity profiles at  $x = 1$  meter and  $Re = 10,000$  obtained from 1000 Monte Carlo realizations are shown in Figure 8.3. An enlarged view is displayed on the right so that the single prediction confidence intervals can be readily observed. The FOSM and SOSM confidence intervals coincide with the Monte Carlo confidence intervals and were omitted in the plot for clarity. It is worth noting that the 95% mean confidence intervals are smaller by a factor of roughly 30 ( $\approx \sqrt{1000}$ ) and should be used for giving the best estimate of the mean. However, since moment-based methods only estimate the standard deviation of the parent population, a more direct comparison to Monte Carlo is afforded by the single prediction confidence intervals.

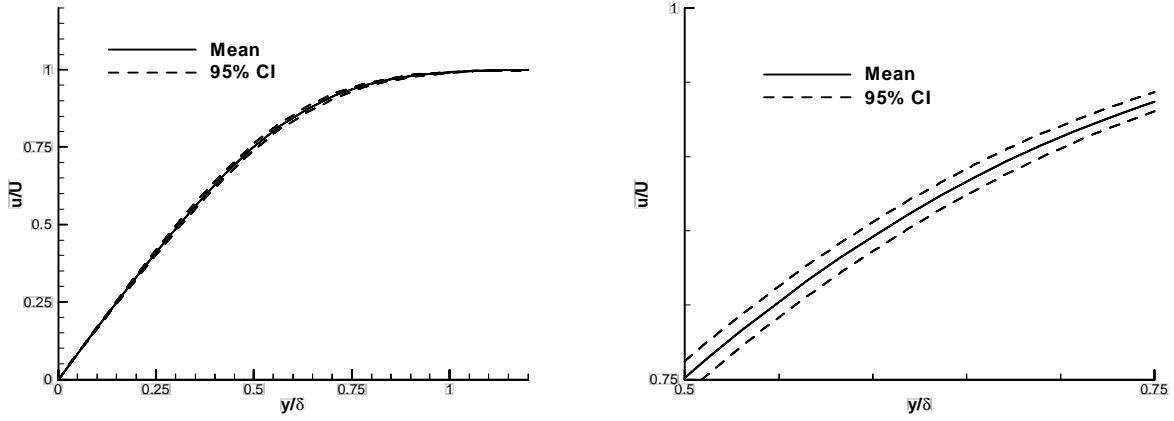


FIG. 8.3. Velocity profiles through the boundary layer with 95% single prediction confidence intervals.

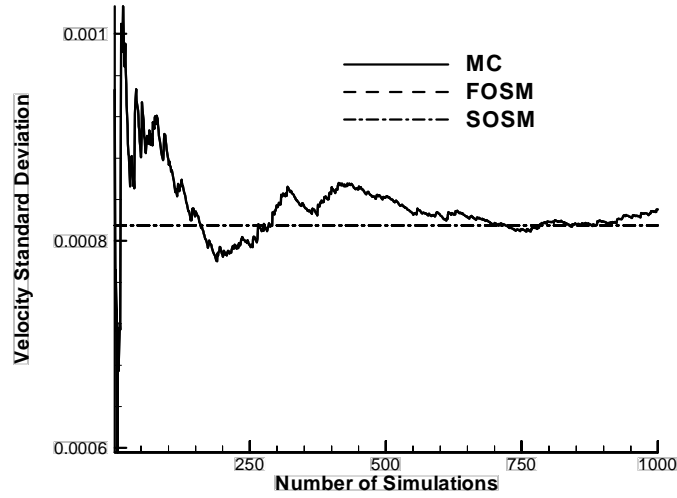


FIG. 8.4. Convergence of Monte Carlo simulations at  $y = 0.17$  meters.

The convergence of the standard deviation predicted by the Monte Carlo method versus the number of simulations is shown in Figure 8.4. The FOSM and SOSM estimates (which lay on top of one another) are also shown. Note the relatively slow convergence of the Monte Carlo method as can be seen by the low frequency meandering of the velocity standard deviation. If one wants very accurate estimates of the standard deviation, this slow convergence and hence high cost will be unacceptable. However, if one only needs a moderately accurate estimate of the mean and is willing to accept a fairly rough estimate of the standard deviation, then relatively few simulations may yield acceptable results.

**9. Summary.** This paper reviews deterministic and probabilistic uncertainty analysis methods applied to fundamental problems in fluid mechanics. Sources of uncertainty and a discussion of selected methods for random variable models are presented. Applications presented include a linear convection problem with a source term, a non-linear Burgers equation, supersonic flow over wedges, expansion corners, and a thin

supersonic airfoil as well as incompressible boundary layer flow.

The methods discussed and implemented are: Interval Analysis, Propagation of error using sensitivity derivatives, Monte Carlo simulation, Moment methods and Polynomial Chaos. Although easy to implement, interval analysis often results in maximal error bounds that are quite large. The basic procedure for implementing Monte Carlo is presented next. Although computationally intensive, Monte Carlo solutions are frequently used as a baseline for comparison with other methods since they are known to converge to the exact stochastic solution in the limit of infinite sample size. First- and second-order moment methods, popular because of the relatively low cost and utility in a design environment are covered. These methods generally yield good approximations when the output probability density function is a Gaussian distribution or relatively close to Gaussian. Next, Hermite polynomial chaos is described for solving stochastic problems involving random variables. The most sophisticated of the methods reviewed, polynomial chaos is based on a spectral representation of the uncertainty which is subsequently decomposed into deterministic and random components. Often, highly accurate results are obtainable from this approach at lower cost than Monte Carlo simulations.

All methods were implemented for a non-linear form of the generalized Burgers equation for which we obtained an exact stochastic solution. To mimic the behavior of CFD codes, we used second order spatial differencing and implemented Newton's method to solve the non-linear problem. In all cases, approximately ten iterations were required to achieve machine precision results. Interval analysis error bounds were unacceptably large, even when performed as a single function evaluation outside the iteration loop. Both first- and second-order moment methods produced reasonable estimates of the mean and variance but the second order estimates were substantially better. Polynomial chaos solutions of various orders were generated. The first-order chaos solutions were comparable to the second moment solutions. The third and fourth-order solutions were very accurate and matched the exact PDF of the solution closely at all points in the domain. We also showed that the treatment of boundary conditions and the quality of the grid has an impact on the error convergence as a function of the order of the chaos.

Oblique shocks and expansions were considered in which the flow turning angle and the input Mach number were considered to be random variables. We used the 2 -  $D$  CFD code FLOW.f as well as shock expansion theory to simulate these flows by the Monte Carlo and first-order moment methods. Parametric results showing the impact of correlation among the variables demonstrate the need to have knowledge about the relationship among input random variables. Supersonic flow over a thin cosine shaped airfoil was studied at a variety of angles-of-attack. The thickness of the airfoil is treated as a random variable and the impact of this uncertainty on the lift-to-drag curve is examined.

Finally, we studied incompressible, steady flow over a flat plate, the celebrated Blasius flow, in which the kinematic viscosity was uncertain. The equations were solved in self-similar variables for which the random variable gets folded into the similarity variable. Both moment methods and Monte Carlo simulations were performed. For this example, little difference was observed between the first- and second-moment methods.

## REFERENCES

- [1] D. P. AESCHLIMAN AND W. L. OBERKAMPF, *Experimental methodology for computational fluid dynamics code validation*, AIAA Journal, 36 (1998), pp. 733–741.
- [2] AIAA APPLIED AERODYNAMICS TECHNICAL COMMITTEE, *Drag Prediction Workshop, 19<sup>th</sup> APA Conference*, Anaheim, CA, 2001. <http://www.aiaa.org/tc/apa/dragpredworkshop/dpw.html>.

- [3] *Guide for the verification and validation of computational fluid dynamics simulations*. AIAA Guide G-077-1998, 1998.
- [4] D. A. ANDERSON, J. C. TANNEHILL, AND R. H. PLETCHER, *Computational Fluid Mechanics and Heat Transfer*, Series in computational methods in mechanics and thermal sciences, McGraw-Hill, 1997.
- [5] J. D. ANDERSON, *Modern Compressible Flow*, McGraw-Hill, New York, USA, 1982.
- [6] T. J. BARBER, *Role of code validation and certification in the design environment*, AIAA Journal, 36 (1998), pp. 752–758.
- [7] J. A. BENEK, E. M. KRAFT, AND R. F. LAUER, *Validation issues for engine-airframe integration*, AIAA Journal, 36 (1998), pp. 759–764.
- [8] C. H. BISCHOF, G. F. CORLISS, L. L. GREEN, A. GRIEWANK, K. HAIGLER, AND P. A. NEWMAN, *Automatic differentiation of advanced CFD codes for multidisciplinary design*, Journal on Computing Systems in Engineering, 3 (1993), pp. 625–637.
- [9] G. DAHLQUIST AND A. BJORCK, *Numerical Methods*, Series in computational methods in mechanics and thermal sciences, Prentice-Hall, 1974.
- [10] D. S. DOLLING, *High-speed turbulent separated flows: Consistency of mathematical models and flow physics*, AIAA Journal, 36 (1998), pp. 725–732.
- [11] D. E. TURGEON AND J. BORGGAARD, *Sensitivity and uncertainty analysis for variable property flows*, AIAA-paper 2001-0140, in 39<sup>th</sup> AIAA Aerospace Sciences Meeting and Exhibit, Reno, NV, January, 2001. CD-ROM.
- [12] B. EFRON AND R. J. TIBSHIRANI, *An Introduction to the Bootstrap*, Chapman and Hall, New York, NY, USA, 1993.
- [13] V. E. GARZON AND D. L. DARMOFAL, *Using computational fluid dynamics in probabilistic engineering design*, AIAA paper 2001-2526, in 15th AIAA Computational Fluid Dynamics Conference, June 11-14, 2001.
- [14] R. GHANEM, *Stochastic finite elements with multiple random non-gaussian properties*, Journal of Engineering Mechanics, (1999), pp. 26–40.
- [15] R. GHANEM AND P. D. SPANOS, *Polynomial chaos in stochastic finite elements*, Journal of Applied Mechanics, 57 (1990), pp. 197–202.
- [16] R. G. GHANEM, *Ingredients for a general purpose stochastic finite element formulation*, Computational Methods in Applied Mechanical Engineering, 168 (1999), pp. 19–34.
- [17] R. G. GHANEM AND P. D. SPANOS, *Stochastic Finite Elements: A Spectral Approach*, Springer-Verlag, New York, 1991.
- [18] A. G. GODFREY, *Topics on Spatially High-Order Accurate Methods and Preconditioning for the Navier-Stokes Equations with Finite-Rate Chemistry*, PhD thesis, Virginia Tech, 1992.
- [19] A. G. GODFREY AND E. M. CLIFF, *Sensitivity equations for turbulent flows*, AIAA-paper 2001-1060, in 39<sup>th</sup> AIAA Aerospace Sciences Meeting and Exhibit, Reno, NV, January, 2001. CD-ROM.
- [20] L. L. GREEN, P. A. NEWMAN, AND K. HAIGLER, *Sensitivity derivatives for advanced CFD algorithm and viscous modeling parameters via automatic differentiation*, Journal of Computational Physics, 125 (1996), pp. 313–324.
- [21] W. G. HABASHI, J. DOMPIERRE, Y. BOURGAULT, M. FORTIN, AND M. WALLET, *Certifiable computational fluid dynamics through mesh optimization*, AIAA Journal, 36 (1998), pp. 703–711.
- [22] A. HALDAR AND S. MAHADEVAN, *Probability, Reliability and Statistical Methods in Engineering Design*,



John Wiley and Sons, Inc., 2000.

- [23] A. HALL, *On an experimental determination of  $\pi$* , Messeng. Math., 2 (1873), pp. 113–114.
- [24] J. M. HAMMERSLEY AND D. C. HANDSCOMB, *Monte Carlo Methods*, Methuen's Monographs on Applied Probability and Statistics, Fletcher & Son Ltd., Norwich, 1964.
- [25] J. C. HELTON AND F. J. DAVIS, *Sampling-based methods for uncertainty and sensitivity analysis*, Tech. Report SAND99-2240, Sandia National Laboratories, July 2000.
- [26] L. HUYSE, *Free-form airfoil shape optimization under uncertainty using maximum expected value and second-order second-moment strategies*, tech. report, ICASE Report 2001-18/NASA CR 2001-211020, 2001.
- [27] ———, *Solving Problems of Optimization Under Uncertainty as Statistical Decision Problems*, AIAA-Paper 2001-1519, in 42<sup>nd</sup> AIAA/ASME/ASCE/AHS/ASC Structures, Structural Dynamics, and Materials Conference and Exhibit, Seattle, WA, 2001.
- [28] L. HUYSE AND R. M. LEWIS, *Aerodynamic shape optimization of two-dimensional airfoils under uncertain conditions*, tech. report, ICASE Report 2001-1/NASA CR 2001-210648, 2001.
- [29] L. HUYSE AND R. W. WALTERS, *Random field solutions including boundary condition uncertainty for the steady-state generalized burger equation*, tech. report, ICASE Report 2001-35/NASA CR 2001-211239, 2001.
- [30] A. JAMESON AND L. MARTINELLI, *Mesh refinement and modeling errors in flow simulations*, AIAA Journal, 35 (1998), pp. 676–686.
- [31] L. KELVIN, *Nineteenth century clouds over the dynamical theory of heat and light*, Phil. Mag., 2 (1901), pp. 1–40.
- [32] M. D. MCKAY, R. J. BECKMAN, AND W. J. CONOVER, *A comparison of three methods of selecting values of input variables in the analysis of output from a computer code*, Technometrics, 21 (1979), pp. 239–245.
- [33] U. B. MEHTA, *Credible computational fluid dynamics simulations*, AIAA Journal, 36 (1998), pp. 665–667.
- [34] E. J. NIELSEN, *Aerodynamic Design Sensitivities on an Unstructured Mesh Using the Navier-Stokes Equations and a Discrete Adjoint Formulation*, PhD thesis, Virginia Tech, December 1998.
- [35] W. OBERKAMPF, J. HELTON, AND K. SENTZ, *Mathematical Representation of Uncertainty*, AIAA Paper 2001-1645, in 42<sup>nd</sup> AIAA/ASME/ASCE/AHS/ASC Structures, Structural Dynamics, and Materials Conference and Exhibit, Seattle, WA, 2001. CD-ROM.
- [36] W. L. OBERKAMPF AND F. G. BLOTTNER, *Issues in computational fluid dynamics code verification and validation*, AIAA Journal, 36 (1998), pp. 687–695.
- [37] M. M. PUTKO, P. A. NEWMAN, A. C. TAYLOR III, AND L. L. GREEN, *Approach for Uncertainty Propagation and Robust Design in CFD Using Sensitivity Derivatives*, AIAA Paper 2001-2528, in AIAA 15<sup>th</sup> Computational Fluid Dynamics Conference, Anaheim, CA, June 2001.
- [38] H. L. REED, T. S. HAYNES, AND W. S. SARIC, *Computational fluid dynamics validation issues in transition modeling*, AIAA Journal, 36 (1998), pp. 742–751.
- [39] A. RIZZI AND J. VOS, *Toward establishing credibility in computational fluid dynamic simulations*, AIAA Journal, 36 (1998), pp. 668–675.
- [40] P. J. ROACHE, *Quantification of uncertainty in computational fluid dynamics*, Annual Review of Fluid Mechanics, 29 (1997), pp. 123–160.
- [41] ———, *Verification of codes and calculations*, AIAA Journal, 36 (1998), pp. 696–702.

- [42] D. G. ROBINSON, *Survey of probabilistic methods used in reliability, risk, and uncertainty analysis: Analytical techniques*, Tech. Report SAND-98-1189, Sandia National Laboratories, June 1998.
- [43] C. J. ROY, *Grid Convergence Error Analysis for Mixed-Order Numerical Schemes*, AIAA Paper 2001-2606, in AIAA 15<sup>th</sup> Computational Fluid Dynamics Conference, Anaheim, CA, June 2001.
- [44] A. C. TAYLOR, L. L. GREEN, P. A. NEWMAN, AND M. M. PUTKO, *Some Advanced Concepts in Discrete Aerodynamic Sensitivity Analysis*, AIAA Paper 2001-2529, in AIAA 15<sup>th</sup> Computational Fluid Dynamics Conference, Anaheim, CA, June 2001.
- [45] F. M. WHITE, *Viscous Fluid Flow*, McGraw-Hill, Inc., 1974.
- [46] S. WOLFRAM, *The Mathematica Book*, Wolfram Media, Cambridge University Press, fourth ed., 1999.
- [47] D. XIU AND G. E. KARNIADAKIS, *Modeling uncertainty in flow simulations via generalized polynomial chaos*, Journal of Computational Physics, (2001). in review.
- [48] ———, *The Wiener – Askey polynomial chaos for stochastic differential equations*, Tech. Report 01-1, Center for Fluid Mechanics, Division of Applied Mathematics, Brown University, Providence, RI, 2001.
- [49] H. C. YEE AND P. K. SWEBY, *Aspects of numerical uncertainties in time marching to steady-state numerical solutions*, AIAA Journal, 36 (1998), pp. 712–724.

REPORT DOCUMENTATION PAGE			Form Approved OMB No. 0704-0188	
Public reporting burden for this collection of information is estimated to average 1 hour per response, including the time for reviewing instructions, searching existing data sources, gathering and maintaining the data needed, and completing and reviewing the collection of information. Send comments regarding this burden estimate or any other aspect of this collection of information, including suggestions for reducing this burden, to Washington Headquarters Services, Directorate for Information Operations and Reports, 1215 Jefferson Davis Highway, Suite 1204, Arlington, VA 22202-4302, and to the Office of Management and Budget, Paperwork Reduction Project (0704-0188), Washington, DC 20503.				
1. AGENCY USE ONLY (Leave blank)		2. REPORT DATE February 2002		3. REPORT TYPE AND DATES COVERED Contractor Report
4. TITLE AND SUBTITLE Uncertainty analysis for fluid mechanics with applications			5. FUNDING NUMBERS  C NAS1-97046 WU 505-90-52-01	
6. AUTHOR(S) Robert W. Walters and Luc Huyse				
7. PERFORMING ORGANIZATION NAME(S) AND ADDRESS(ES) ICASE Mail Stop 132C NASA Langley Research Center Hampton, VA 23681-2199			8. PERFORMING ORGANIZATION REPORT NUMBER  ICASE Report No. 2002-1	
9. SPONSORING/MONITORING AGENCY NAME(S) AND ADDRESS(ES) National Aeronautics and Space Administration Langley Research Center Hampton, VA 23681-2199			10. SPONSORING/MONITORING AGENCY REPORT NUMBER NASA/CR-2002-211449 ICASE Report No. 2002-1	
11. SUPPLEMENTARY NOTES Langley Technical Monitor: Dennis M. Bushnell Final Report				
12a. DISTRIBUTION/AVAILABILITY STATEMENT  Unclassified-Unlimited Subject Category 64 Distribution: Nonstandard Availability: NASA-CASI (301) 621-0390			12b. DISTRIBUTION CODE	
13. ABSTRACT (Maximum 200 words) This paper reviews uncertainty analysis methods and their application to fundamental problems in fluid dynamics. Probabilistic (Monte-Carlo, Moment methods, Polynomial Chaos) and non-probabilistic methods (Interval Analysis, Propagation of error using sensitivity derivatives) are described and implemented. Results are presented for a model convection equation with a source term, a model non-linear convection-diffusion equation; supersonic flow over wedges, expansion corners, and an airfoil; and two-dimensional laminar boundary layer flow.				
14. SUBJECT TERMS stochastic, probabilistic, uncertainty, error			15. NUMBER OF PAGES 50	
			16. PRICE CODE A03	
17. SECURITY CLASSIFICATION OF REPORT Unclassified	18. SECURITY CLASSIFICATION OF THIS PAGE Unclassified	19. SECURITY CLASSIFICATION OF ABSTRACT	20. LIMITATION OF ABSTRACT	